Electronic Thesis and Dissertation Repository

9-5-2014 12:00 AM

Prostate Tumor Volume Measurement on Digital Histopathology and Magnetic Resonance Imaging

Mehrnoush Salarian, *The University of Western Ontario*

Supervisor: Dr. Aaron D Ward, *The University of Western Ontario*
A thesis submitted in partial fulfillment of the requirements for the Master of Engineering
Science degree in Biomedical Engineering
© Mehrnoush Salarian 2014

Follow this and additional works at: https://ir.lib.uwo.ca/etd

🅖 Part of the Biomedical Engineering and Bioengineering Commons

PROSTATE TUMOUR VOLUME MEASUREMENT ON DIGITAL HISTOPATHOLOGY AND MAGNETIC RESONANCE IMAGING

(Thesis format: Integrated Article)

by

Mehrnoush <u>Salarian</u>

Graduate Program in Biomedical Engineering

A thesis submitted in partial fulfillment
of the requirements for the degree of
Master of Science Engineering

The School of Graduate and Postdoctoral Studies
The University of Western Ontario
London, Ontario, Canada

Abstract

An accurate assessment of prostate tumour burden supports appropriate treatment selection, ranging from active surveillance through focal therapy, to radical whole-prostate therapies. For selected patients, knowledge of the three-dimensional locations and sizes of prostate tumours on pre-procedural imaging supports planning of effective focal therapies that preferentially target tumours, while sparing surrounding healthy tissue. In the post-prostatectomy context, pathologic measurement of tumour burden in the surgical specimen may be an independent prognostic factor determining the need for potentially life-saving adjuvant therapy. An accurate and repeatable method for tumour volume assessment based on histology sections taken from the surgical specimen would be supportive both to the clinical workflow in the post-prostatectomy setting and to imaging validation studies correlating tumour burden measurements on pre-prostatectomy imaging with reference standard histologic tumour volume measurements.

Digital histopathology imaging is enabling a transition to a more objective quantification of some surgical pathology assessments, such as tumour volume, that are currently visually estimated by pathologists and subject to inter-observer variability. Histologic tumour volume measurement is challenged by the traditional 3–5 mm sparse spacing of images acquired from sections of radical prostatectomy specimens. Tumour volume estimates may benefit from a well-motivated approach to inter-slide tumour boundary interpolation that crosses these large gaps in a smooth fashion. This thesis describes a new level set-based shape interpolation method that reconstructs smooth 3D shapes based on arbitrary 2D tumour contours on digital histology slides. We measured the accuracy of this approach and used it as a reference standard against which to compare previous approaches in the literature that are simpler to implement in a clinical workflow, with the aim of determining a method for histologic tumour volume estimation that is both accurate and amenable to widespread implementation. We also measured the effect of decreasing inter-slide spacing on the repeatability of histologic tumour volume estimation. Furthermore, we used this histologic reference standard for tumour volume to measure the accuracy, inter-observer variability, and inter-sequence variability of prostate

tumour volume estimation based on radiologists' contouring of multi-parametric magnetic resonance imaging (MPMRI).

Our key findings were that (1) simple approaches to histologic tumour volume estimation that are based on 2- or 3-dimensional linear tumour measurements are more accurate than those based on 1-dimensional measurements; (2) although tumour shapes produced by smooth through-slide interpolation are qualitatively substantially different from those obtained from a planimetric approach normally used as a reference standard for histologic tumour volume, the volumes obtained were similar; (3) decreasing inter-slide spacing increases repeatability of histologic tumour volume estimates, and this repeatability decreases rapidly for inter-slide spacing values greater than 5 mm; (4) on MPMRI, observers consistently overestimated tumour volume as compared to the histologic reference standard; and (5) inter-sequence variability in MPMRI-based tumour volume estimation exceeded inter-observer variability.

Keywords: Prostate cancer, digital histopathology, radical prostatectomy, tumour volume, level set method, shape interpolation, multi-parametric magnetic resonance imaging.

Co-Authorship Statement

The work in Chapter 2 has been prepared for submission to the SPIE Journal of Medical Imaging, under the title, "Toward Quantitative Digital Histopathology for Prostate Cancer: Comparison of Inter-slide Interpolation Methods for Tumour Measurement," by Salarian M., Shahedi M., Gibson E., Gaed M., Gomez J. A., Moussa M., Cool D. W., Romagnoli C., Bauman G. S., and Ward A. D.

The work in Chapter 3 has been published in the proceedings of the SPIE Medical Imaging Conference, San Diego, California, USA, Vol 9041, 90410I, 2014, under the title, "Accuracy and variability of tumour burden measurement on multi-parametric MRI," by Salarian M., Gibson E., Shahedi M., Gaed M., Gomez J. A., Moussa M., Romangnoli C., Cool D. W., Bastian-Jordan M., Chin J., Bauman G. S., and Ward A. D.

My contributions to both chapters were the manipulation and analysis of the 2D digital histology and 3D MRI images, processing the data, and the writing of the manuscripts. All of these activities were performed under the supervision and advice of Dr. Aaron Ward. He led the project by defining the research theme, providing guidance, and editing the manuscripts. Dr. Bauman and Dr. Fenster provided advice and recommendations during advisory committee meetings.

Dr. Romagnoli, Dr. Cool and Dr. Bastian-Jordan assessed and contoured the MPMRI images, and Dr. Gaed contoured and graded the tumours on the digital histology images under the supervision of Dr. Gomez and Dr. Moussa. Eli Gibson designed and implemented the MRI-histology co-registration algorithm.

Dedication

To people whose love and support make my life meaningful:

my parents and my sister.

Acknowledgments

First and foremost, I would like to express my deep gratitude to Dr. Aaron Ward for his tremendous guidance, support and confidence in me. The completion of this dissertation would not have been possible without his incomparable assistance and invaluable effort.

No matter how busy, he always made time to answer my questions and afforded me endless patience and encouragement. I learned a great deal from him and was inspired by his passion for science and innovation. It was truly an honour to be one of his students, and to be a part of his lab.

I would like to gratefully thank Maysam Shahedi for his guidance and help and for the hours Maysam spent in helping me in processing data and answering my questions. He always seemed more than happy to help me. Also, I would like to express my appreciation to Eli Gibson for his help and hard work on data acquisition and doing the registration task.

I would like to acknowledge my advisory committee members, Dr. Glenn Bauman and Dr. Aaron Fenster for their insight, feedback, and recommendations.

Additionally, I would also thank all my colleagues in the Baines Lab for their support, help and cooperation. Also, I acknowledge my true friend Sahar for her love, friendship and support.

Finally, words are not enough to express my gratitude towards my family. Without the unconditional love, encouragement, tremendous patience and understanding of my parents, Mohammadreza and Minoo, and my beloved sister, Mehrnaz I would not have been able to accomplish my goals.

Table of Contents

List of Tables

List of Figures

List of Abbreviations, Symbols, Nomenclature

Abbreviations

ADC	Apparent diffusion coefficient
BCF	Biochemical failure
BPH	Benign prostatic hyperplasia
CT	Computed tomography
CZ	Central zone
CV	Cubic volume
DCE	Dynamic contrast enhanced
DRE	Digital rectal examination
1D	One dimensional
2D	Two dimensional
3D	Three dimensional
ECE	Extra capsular extension
ESA	Estimated square area
HIFU	High-intensity focused ultrasound
LS	Level set
MRI	Magnetic resonance imaging
MTD	Maximum tumour diameter
NN	Nearest neighbour
PCa	Prostate cancer
PIN	Prostatic intraepithelial neoplasia
PSA	Prostate-specific antigen
PZ	Peripheral zone
RP	Radical prostatectomy
SVI	Seminal vesicle invasion
T2W	T2-weighted
TRUS	Transrectal ultrasound
TV	Tumour volume
TZ	Transition zone

Chapter 1

1 General introduction and literature review

1.1 Motivation and clinical overview

Prostate cancer (PCa) is the most common non- cutaneous cancer and the second leading cause of cancer death among men. One in seven Canadian men will likely develop PCa within his lifetime. It is estimated that in 2014, 23,600 men will be diagnosed with PCa and 4,000 men will die of PCa in Canada [1]. Most PCa is typically slow-growing, which means that it takes several years to become large enough to be detectable and men who develop PCa may live many years without any symptoms. It is important that screening is done regularly in men so that if they develop PCa, appropriate action can be taken. In addition, if PCa is detected at an early stage, it is highly treatable and in most cases, curable [2]. Screening based on serum prostate-specific antigen (PSA) testing and digital rectal examination (DRE), followed by 2D transrectal ultrasound (TRUS)-guided biopsy has resulted in the detection of tumours at an earlier stage.

However, due in part to the high sensitivity and low specificity PSA testing and sampling issues related to 2D TRUS-guided biopsy, PCa is currently considered to be an over-diagnosed disease [3]. This potentially leads to aggressive whole-gland therapies (radical radiotherapy or prostatectomy surgery) with associated life-changing side effects. On the other hand, there is a 40% rate of discrepancy between the Gleason grade estimated at biopsy and the true grade at prostatectomy [4, 5]. In cases where the grade is underestimated, the patient could be incorrectly placed on active surveillance, with the psychological burden related to untreated PCa [3, 6]. After a patient has been diagnosed with PCa, many challenges exist regarding treatment. The first is the selection of appropriate treatment for each individual patient. The second is, for patients who undergo radical prostatectomy surgery to remove the prostate, determining whether additional treatment is needed, and if so, when to apply this treatment. The flow diagram in Figure 1.1 shows some of the treatment options for organ-confined PCa.
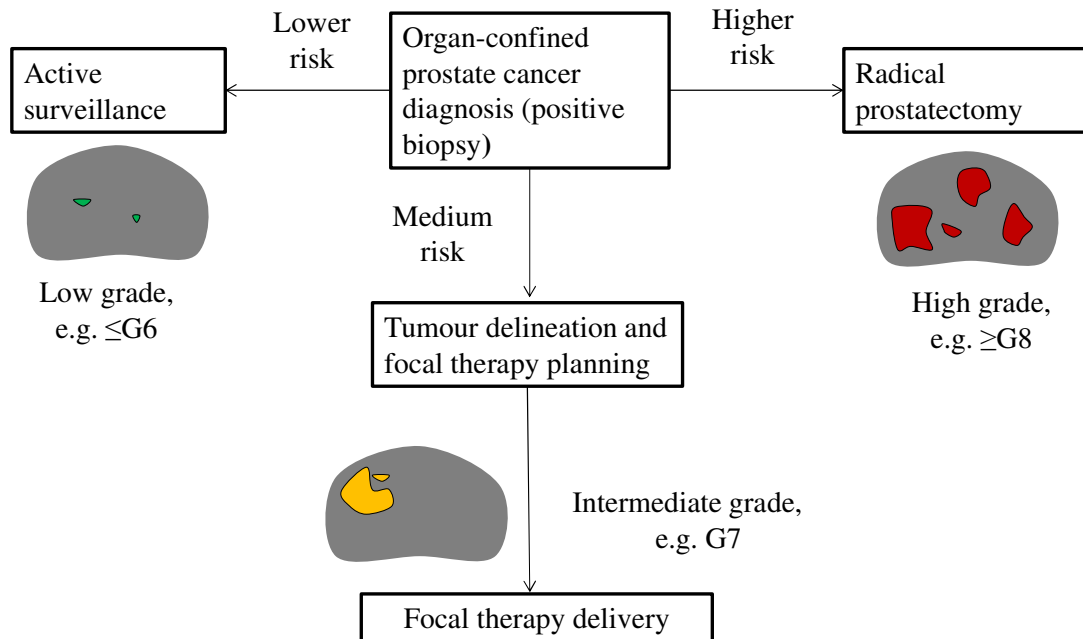
Figure 1.1. Schematic diagram showing some of the treatment options for organ-confined prostate cancer.

There are several different therapeutic modalities for organ-confined prostate cancer treatment, with the appropriate choice depending on the risk level of the patient. Active surveillance may be appropriate if the cancer is small, low-grade, expected to be slow-growing, and confined to one area of the prostate. During active surveillance, PCa is monitored closely for any changes and no immediate treatment may be required. As there are no invasive procedures and drugs used, there are no immediate side effects from active surveillance. However, patients on active surveillance can feel anxiety regarding the lack of treatment for their cancer, and may be concerned about the potential for their cancer to change into a more life-threatening form. For higher risk patients, radical prostatectomy (RP) may be needed. RP is a surgical procedure to remove the prostate gland plus a margin of tissue around it, including the seminal vesicles. In cases of truly organ-confined cancer with a clear surgical margin, RP has the advantage of total excision of the cancerous tissue from the patient. However, RP has side effects including erectile dysfunction and urinary incontinence. It has been estimated that approximately

40% of men with organ-confined PCa undergo RP, with nearly 80,000 surgeries per year in the United States [7]. For medium risk patients with tumours localized to specific regions within the prostate, focal therapy may be appropriate. Focal therapy is an emerging type of treatment and may serve as a middle ground between active surveillance and RP for patients with low to intermediate-risk cancers [8]. It involves the treatment of only the dominant intraprostatic lesion(s), while minimizing damage to surrounding healthy tissue. However, focal therapy is not currently used routinely in the clinical workflow [7].

It has been shown that for approximately 35% of patients who underwent RP, there was evidence of recurrence as measured by an increase in the PSA level (beyond 0.2 ng/mL) in the blood [9]. This is known as biochemical failure, or BCF. After BCF, it may be possible to cure the patient by applying salvage therapy, using modalities including radiation, salvage RP (in cases of failure of primary radiation therapy), cryoablation, and high-intensity focused ultrasound (HIFU). If BCF is anticipated based on adverse findings on surgical pathology, adjuvant therapy may be applied shortly after RP. In adjuvant therapy, the physician does not wait for BCF to occur; therapy is applied as soon as possible after RP surgery. Therefore, the pathologist's assessment of the surgically removed prostate may identify the need for adjuvant therapy [10]. If the pathology report contains findings that suggest strongly that the cancer may recur, such as one or more large-volume tumours, adjuvant therapy may be indicated.

The decision of whether to use adjuvant therapy is important and challenging. Adjuvant therapy cannot be used for all patients due to the serious side effects that can occur, but can be life-saving for appropriately selected patients. Planning of post-prostatectomy adjuvant or salvage treatment depends on tumour volume (TV), Gleason grades of the tumours, and the focality and location of the tumours in the prostatectomy specimen [11]. In addition, planning for focal therapy requires that the tumour targets be delineated on imaging, with a suitable margin to account for treatment delivery uncertainty, and there are currently no generally accepted guidelines for physicians to follow in doing this task. An accurate and repeatable assessment of tumour volume in the prostatectomy specimen would be valuable to therapy selection for RP patients, and also

useful to imaging-histology co-registration approaches to the determination of suitable treatment margins for focal therapy [12-14].

1.2 The prostate gland

1.2.1   Anatomy and physiology

The normal prostate gland is about the size of a walnut and somewhat conical in shape within the male reproductive system. It is located in front of the rectum and directly beneath the bladder (Figure 1.2 (a)). The main function of the prostate is to produce fluid that forms part of the semen. On both sides of the prostate are neurovascular bundles which, if damaged during cancer treatment (e.g. surgery, radiation therapy), could lead to erectile dysfunction (Figure 1.2 (b)) [15].
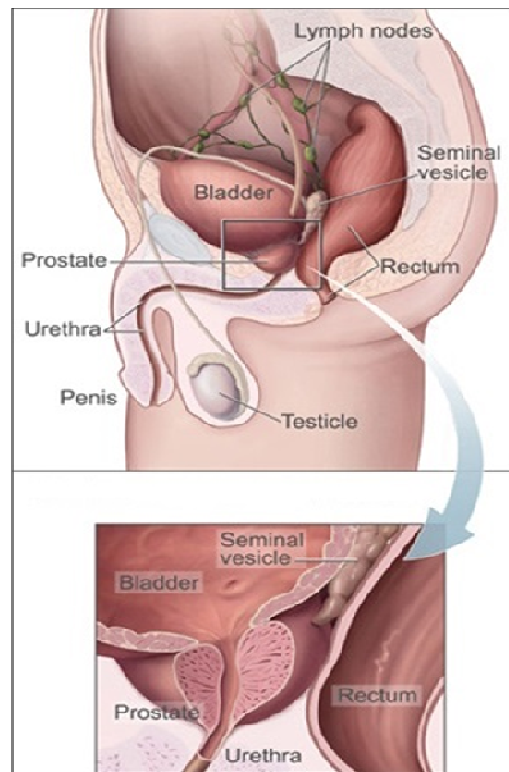
Figure 1.2. (a) Sagittal view of prostate and nearby organs, depicting its position relative to the bladder. (b) Sagittal view of prostate showing the inside of the prostate, urethra, rectum, and bladder [16].

The prostate is divided into three distinct anatomical regions. The peripheral zone (PZ) covers 70% of the glandular prostate. It is located in the outer area of the prostate, close to the rectum. The central zone (CZ) constitutes 25% of the glandular prostate. It is located in the center of the prostate with its base at the bladder neck and its tip at the verumontanum. Finally, the transition zone (TZ) covers 5% of the glandular prostate. It is above the CZ and also includes two lobes located anteriorly between the proximal urethra and the lateral parts of the PZ (Figure 1.3). Most studies have shown that the PZ is the most common site for prostate cancer foci, whereas common abnormalities such as benign prostatic hyperplasia (BPH) develop mainly in the CZ and TZ [17]. BPH symptoms are often similar to cancer; however BPH involves the noncancerous enlargement of the prostate gland and typically occurs in older men. If the prostate's size grows too large, it may press on the bladder, causing frequent urination, or it may constrict the urethra and impede urine flow [15].
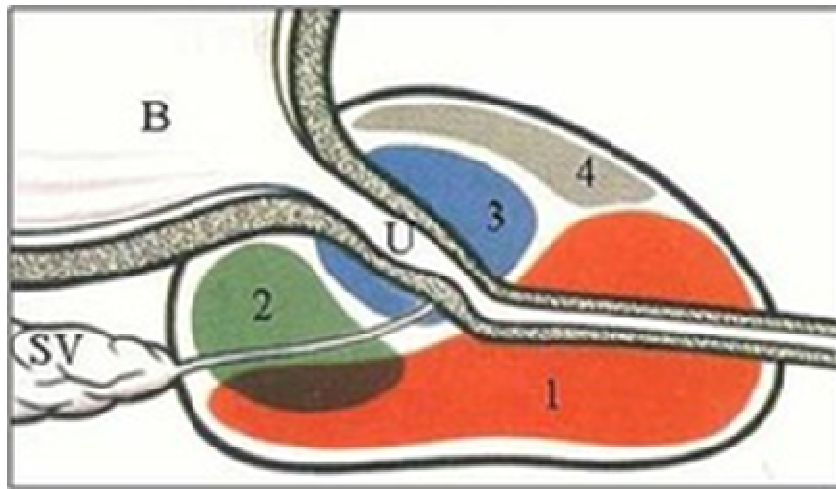
Figure 1.3. Schematic diagram depicting the prostate zones in the sagittal plane. 1 = PZ (peripheral zone), 2 = CZ (central zone), 3 = TZ (transitional zone), 4 = anterior fibromuscular zone, B = bladder, and U = urethra [18].

1.2.2 Prostate cancer

PCa results from an oncogenic, or dysplastic, change in the prostate glandular tissue. The tumour foci are often microscopic and heterogeneous [2]. PCa is typically a slow growing cancer and some men who develop PCa may live many years without having any cancer detected. However, there are cases of aggressive PCa where cancer cells may metastasize from the prostate to other parts of the body. PCa is mostly asymptomatic in its early stages, however other symptoms can arise during later stages, which cause frequent urination, blood in the urine, and pain in urinating. Urinary dysfunction is associated with the fact that the prostate gland surrounds the urethra. Consequently, any changes within the gland (including prostate enlargement) can directly affect urinary function and can pinch off the urethra and/or generate pressure on the bladder (Figure 1.4). Cancerous growth in the prostate can either be benign or malignant. PCa is generally considered to be a malignant tumour and the prostate tends to enlarge asymmetrically in the presence of PCa. However, in BPH, the prostate mainly tends to enlarge centrally, and the prostate shape remains more uniform.
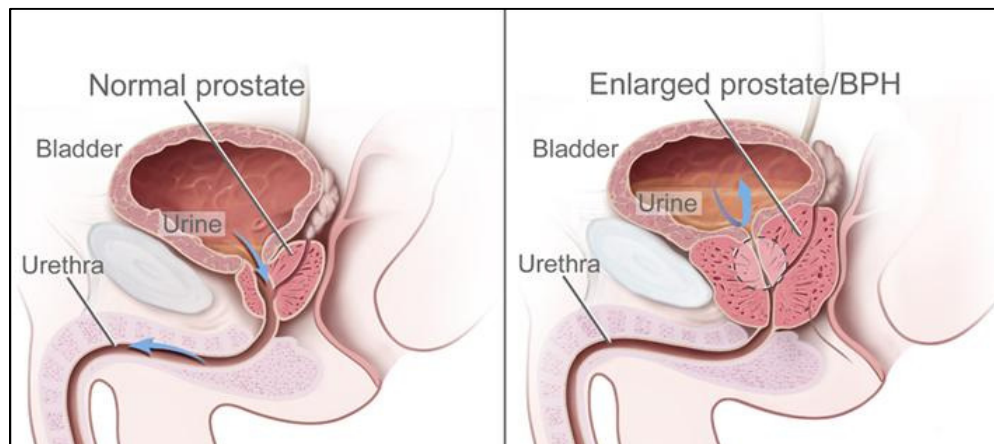
Figure 1.4. Schematic diagram depicting a normal prostate and a prostate enlarged due to BPH. A normal prostate does not block urine flow from the bladder, whereas an enlarged prostate blocks urine flow and presses on the urethra and bladder [19].

1.2.3 Prostate cancer screening

Early detection and accurate preoperative assessment of prostate cancer are essential to the selection of appropriate treatment [20]. Since if cancer is detected too late, it may become exophytic and subsequently metastasize to the rest of the body, some screening tests such as PSA, DRE and 2D TRUS-guided biopsy have been used to detect the presence of cancer in its earliest stages. The PSA test measures the amount of PSA in the blood. PSA was first identified in seminal fluid by Hara in 1969 [21]. This antigen is produced within the prostate gland and is found in the blood in very small concentrations. Higher blood levels of PSA may occur in the presence of cancer and can also indicate other prostate conditions such as BPH. The normal range for PSA is generally considered to be 0 to 4 ng/ml [22]. However, more recent studies have shown that the PSA test is not specific to PCa and many men with higher PSA levels do not have prostate cancer; this can lead to false-positive results. Some men with PSA levels below 4 ng/ml have prostate cancer; this can lead to false-negative results [1, 22, 23]. In most cases, the patient is referred for further investigation (e.g. biopsy) when PSA levels rise above 4 ng/ml [24].
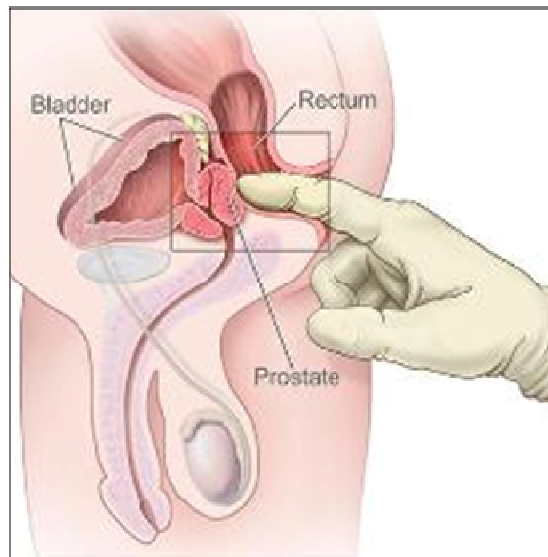
Figure 1.5. Schematic diagram depicting the digital rectal exam [26].

A DRE is a physical examination performed by manual palpation of the prostate to detect any irregularities in size, shape, and texture, in an effort to distinguish PCa and non-cancerous conditions such as BPH. In the DRE test, the physician inserts a gloved

finger into the rectum to palpate the prostate gland; during the test, the patient may feel temporary discomfort. The DRE test is not very sensitive for detection of small, early-stage tumours. Furthermore, it is limited by the physician's access to mainly the posterior portion of the gland (Figure 1.5) [25]. If the result of the DRE test is abnormal, further testing is required to determine whether cancer is present.

Both the DRE and PSA tests are very easy to perform, inexpensive, require little time, and are not associated with any significant risks. PCa detected as a result of PSA screening is often at an earlier, more treatable stage.

A 2D transrectal ultrasound (TRUS)-guided prostate biopsy (Figure 1.6) is the clinical standard for diagnosis, and is usually employed when the results of a DRE and/or PSA test are suspicious for cancer. It is performed by inserting an end-firing or side-firing ultrasound transducer probe into the patient's rectum to acquire prostate images by manipulating the transducer probe against the rectal wall. Once the probe is positioned, a biopsy needle loaded into a biopsy gun is attached to the probe through a needle guide that keeps the needle with in the 2D imaging plane of the transducer. A small biopsy "core" of tissue is sampled near the needle tip when the biopsy gun is fired, and these tissue cores are sent for histopathological analysis to detect and grade cancer. The standard needle size is 18 gauge (1.2 mm outer diameter, 1.0 mm inner diameter) [27].

A typical pattern of biopsy targets is the sextant (Figure 1.7), wherein six biopsies are taken from the right and left upper, middle, and lower lobes [26]. 2D TRUS has limitations of poor cancer visualization and biopsy guidance, contributing to a reported false negative rate of 34% [27]. It has become clear that TRUS imaging may not be sufficient for prostate biopsy target localization, and it is worthwhile to explore alternative imaging modalities for this purpose.
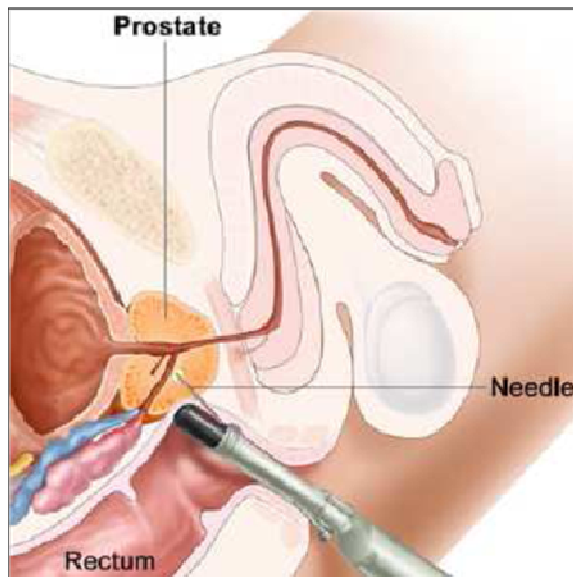
Figure 1.6. Schematic diagram depicting the TRUS-guided biopsy procedure (courtesy of the National Cancer Institute, USA) [19].

It has been shown that in many men with PCa, significant cancer was missed on initial biopsy sampling, motivating more extensive sampling of the prostate to exclude under-sampled significant cancer [29]. Although there is no controversy that tumour volume in needle biopsy specimens should be reported, there is no consensus regarding which method of tumour quantification should be adopted [30]. A single biopsy session yields approximately 12 cylindrical 1 mm × 18 mm tissue samples and therefore provides a tenuous estimate of tumour burden only under a strong set of assumptions. Emerging evidence suggests that imaging may permit accurate assessment of PCa burden with implications for screening and targeting treatment [31]. These challenges motivate the need to assess tumour volume better on imaging, which is the focus of the work described in Chapter 3.
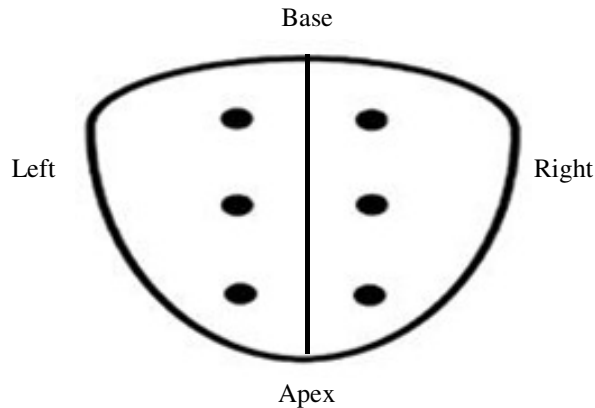
Figure 1.7. A diagram of the prostate, viewed from the posterior side, to illustrate sextant biopsy [32].

1.3 Prostate cancer tumours

1.3.1 Prostate cancer tumour volume for prognosis

Many studies of PCa have investigated the relationship between tumour size/volume measurement and prognosis. Histopathological analysis of PCa features in RP specimens provides information that can predict the future course of the disease [33-35]. After RP, standard prognostic parameters regarding PCa progression include the overall Gleason score [36], the presence of extracapsular extension (ECE), seminal vesicle invasion (SVI), pathological staging, status of the surgical margins, and tumour volume [37]. In some studies, some of these predictors have been shown to be related, such as the Gleason grade and tumour volume, and the margin status and pathological stage [38, 39]. However, the question of whether tumour volume is an independent prognostic factor has remained controversial [40-42]. Some studies have shown that tumour volume is an independent prognostic parameter and recommend its use for supporting treatment selection [43]. On the other hand, other studies have shown that tumour volume is not able to independently provide additional information regarding cancer progression, if Gleason grade and pathological stage are known [41]. Some studies have failed to demonstrate the significance of tumour volume as an independent prognostic factor [44, 45]. Differences between study cohorts and the use of different methods for tumour volume estimation in different studies could be contributing factors

to these conflicting results regarding tumour volume. If tumour volume was widely considered to be an independent prognostic parameter, pathologists could justify its routine measurement and clinical reporting. However, to determine whether it is indeed an independent prognostic parameter, a standard method for tumour volume measurement that is accurate, repeatable, and can be widely implemented in the clinical workflow is needed. A 2009 International Society of Urological Pathology Consensus Conference included 116 genitourinary pathologists from 23 countries and concluded that, "…in view of the potential importance of tumour size as a prognostic parameter, coupled with the recent advances in imaging technology, it may prove necessary to embrace more sophisticated methods for measuring tumour [size]. This was considered of some importance as some argued that tumour size may become more important as a defining parameter for both clinical and pathological staging." [46].

1.3.2 Prostate cancer tumour volume assessment using 2D digital histopathology imaging

PCa tumour volumes in RP specimens were first reported in 1986 [39]. The traditional RP process includes tissue fixation in 10% buffered formalin for 12–48 hours, followed by slicing into 3–5 mm thick tissue sections which are subsequently embedded in paraffin blocks. 4–5 µm thick sections are then cut with a microtome from each block face for hæmatoxylin and eosin (H&E) staining [47]. The pathologist then conducts a microscopic examination of the sections. Each tumour is characterized in several ways, including by location within the prostate, volume, and degree of differentiation [10]. The pathology report provides essential information on prognostic characteristics relevant for making clinical decisions regarding the need for further treatment.

The advent of whole-slide scanners is ushering in a new era in clinical pathology, permitting the development of a digital environment for the management and assessment of pathological images. Many scanners can digitally scan slides at diagnostic resolution (0.25 µm per pixel) [48], with some scanners capable of higher resolutions of up to 100× magnification (0.14 µm per pixel). Such devices open the possibility for the integration of

computational tools into the digital pathology workflow in order to enable quantitative assessments and enhancing clinical practice [49].

Whole-mount digital histology sections have been proposed as a reference standard for evaluating tumour size, location, grade, and multifocality, and may permit more accurate assessment of tumour volume where conventional sampling by biopsy is difficult. A sample contoured whole-mount histopathology image is shown in Figure 1.8. In the research study from which this slide was obtained, the pathologist contoured and graded (using different coloured contours) all of the lesions on the image, as well as some benign observations.
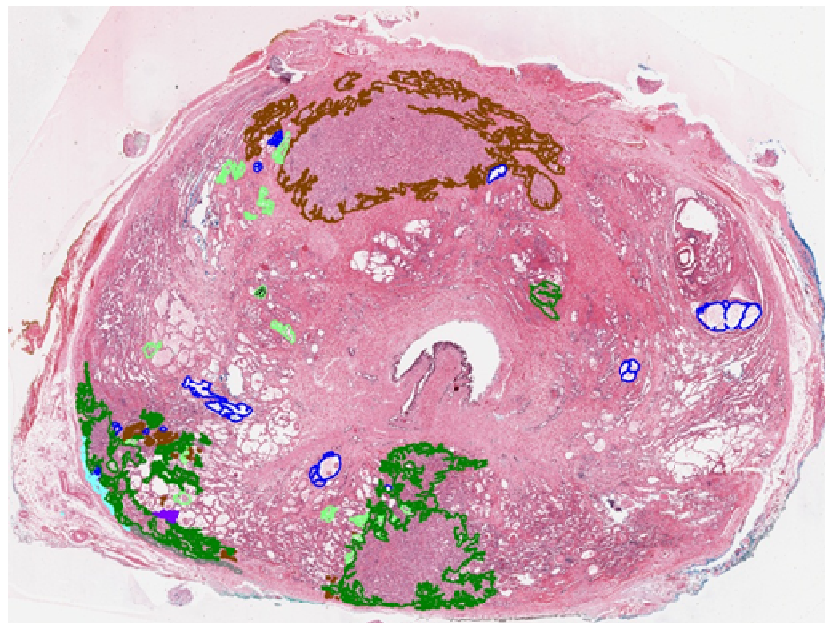
Figure 1.8. Sample contoured whole-mount, H&E-stained histopathology image. Colour code is as follows. Brown: low-grade cancer. Gray, dark green, purple: regions containing several different grades of cancer, all including some high-grade cancer. Cyan: extraprostatic extension of tumour. Blue: atrophy (benign). Light green: prostatic intraepithelial neoplasia (benign).

1.3.3 Prostate cancer tumour volume assessment using magnetic resonance imaging

Although imaging findings alone are not adequate for the primary diagnosis of PCa, it has been shown that imaging could deliver richer 3D information, complementary to the histological diagnosis. Several investigations have suggested that imaging could be able to accurately define tumour margins that would provide tumour localization, size estimation, real-time monitoring, and follow-up [50]. Among current imaging modalities, magnetic resonance imaging (MRI) is gaining acceptance as the best imaging modality for detecting and staging PCa due to the excellent anatomical and functional images that can be obtained [51]. 3 Tesla (T) MRI, with its higher signal-to-noise ratios and higher spatial resolution, has shown better PCa detectability as compared with 1.5 T MRI [52], but the use of 3 T MRI to estimate tumour volume has not been widely assessed.

Multi-parametric MRI (MPMRI), with its morphological and functional pulse sequence capabilities, has been recommended for the accurate assessment of prostate tumour burden. Typical pulse sequences used for PCa imaging include T2-weighted (T2W), diffusion-weighted (DW) and dynamic contrast enhanced (DCE) images [46]. T2W MRI essentially gives anatomical information about the prostate [53], DCE MRI allows the visualization of vascular permeability and perfusion [54], and DW MRI provides information regarding tissue cellular density and membrane integrity [55]. MPMRI has been recommended for PCa diagnosis, localization, and staging [53]. However, the accuracy and inter-observer variability of prostate tumour volume estimation based on separate expert contouring of each of the T2W, DCE, and DW MRI sequences acquired using an endorectal coil at 3 T is relatively under-explored.

1.3.4 Methods for prostate tumour volume measurement

In current clinical practice, prostate tumour volume is assessed visually by pathologists; it is challenging to report quantitatively and is subject to observer variability [46, 56]. 3D quantification is challenged by the conventional 3–5 mm inter-slide spacing which is used in clinical pathology for reasons of cost and a need to archive tissue for future diagnosis [47]. To address this challenge, several methods that are amenable to

implementation in a clinical pathology workflow have been reported previously for prostate tumour volume estimation on histology and are described as follows. (1) Cubic volume (CV) method: tumour volume is estimated as $width \times height \times length$, where $width$ is the length of the greatest diameter the tumour, $height$ is the length of the minor axis across the largest area, and $length$ is calculated by multiplying the inter-slide spacing by the number of slices containing any tumour [57]. (2) Maximum tumour diameter (MTD) method: tumour size is estimated as its $width$ [58]. (3) Estimated square area (ESA) method: tumour size is estimated as $width \times height$. These simple approaches are valuable if they can be shown to be correlated to a trusted measure of tumour volume, since their dependence on only a few linear measurements makes them relatively straightforward to implement in a clinical workflow.

A typically-used reference standard for tumour volume on prostate digital histology requires that the tumour be contoured on every slide on which it appears [59]. Using this method, tumour volume on digital pathology images is estimated as the sum of within-slide tumour areas multiplied by the inter-slide spacing [60]. However, due to the large difference between the slice thickness (4–5 µm) and the slide spacing (3–5 mm), this approach can produce sharp changes in the tumour surface along the direction orthogonal to the slides. As discussed in Section 1.5, one of the objectives of this thesis is to develop a method for prostate tumour shape interpolation that produces smooth and more plausible tumour boundaries.

On MPMRI, two different approaches have been reported previously for prostate tumour volume measurement. (1) 2D slice-by-slice method: After outlining the regions that are suspicious for cancer on each 2D MRI plane on which the tumour appears, the areas of these regions are multiplied by the MRI plane thickness to calculate the tumour volume [61]. (2) 3D method: The boundary of the 3D region that is suspicious for cancer is defined with subvoxel precision by manipulation of the vertices of a 3D triangle mesh enclosing the region. The tumour volume is then estimated as the volume enclosed by the 3D triangle mesh [61].

1.4 Hypothesis

The central hypotheses of this thesis are that (1) tumour size estimates based on the MTD, ESA, and CV methods can be used to obtain accurate estimates of prostate tumour volume on histology; (2) repeatability of histologic tumour volume estimation increases with decreasing inter-slide spacing; and (3) radiologists can accurately and repeatably estimate prostate tumour volume by contouring suspicious regions on MPMRI. Hypotheses (1) and (3) will be tested using the nearest-neighbour approach and a newly-developed level-set based smooth shape interpolator as reference standards on histology imaging.

1.5 Objectives

To test the central hypotheses, this thesis has the following objectives:

1. To develop a method based on a level set shape representation for estimation of smooth 3D prostate tumour shapes, based on sparse tumour contours on 2D histology images.

2. To compare tumour volumes obtained from the level set approach to those obtained using the nearest-neighbour approach, which is typically used as a reference standard.

3. To compare tumour volumes obtained from the MTD, ESA, and CV approaches to tumour volumes obtained from the nearest-neighbour and level-set based approaches.

4. To perform a simulation testing the impact of varying inter-slide spacing on the repeatability of histologic tumour volume estimates.

5. To compare tumour volumes obtained from radiologists' 3D contouring of T2W, DCE, and ADC MR images to corresponding histologic tumour volumes from the same patients.

6. To measure the inter-observer and inter-sequence variability in tumour volumes obtained from radiologists' 3D contouring of T2W, DCE, and ADC MR images.

1.6 Thesis outline

1.6.1 Chapter 2: Evaluation of the difference between inter-slide interpolation methods for prostate tumour measurement on 2D digital histopathology

Digital pathology imaging enables imaging-pathology fusion to validate imaging for focal therapy planning, as well as quantification of surgical pathology assessments such as tumour volume, that are currently visually estimated and subject to observer variability. The computation of tumour volume and shape from digitized images of 4 micron histology sections acquired with 3–5 mm spacing is complicated by this large image spacing:thickness ratio, requiring a plausible through-slide shape interpolation. In this chapter, we describe our developed level set (LS)-based interpolation method that produces smooth interpolations of arbitrary shapes. This chapter addresses objectives 1 through 4 as described in Section 1.5.

A preliminary version of this chapter has been published as "Toward Quantitative Digital Histopathology for Prostate Cancer: Comparison of Inter-Slide Interpolation Methods for Tumour Measurement," by M. Salarian, M. Shahedi, E. Gibson, M. Gaed, J.A. Gomez, M. Moussa, G.S. Bauman, A.D. Ward, in the proceedings of SPIE Medical Imaging 2013.

A full version of this chapter will be submitted as, "Toward Quantitative Digital Histopathology for Prostate Cancer: Comparison of Inter-Slide Interpolation Methods for Tumour Measurement" by Salarian M., Shahedi M., Gibson E., Gaed M., Gomez J. A., Moussa M., Cool, D., Romagnoli, C., Bauman G. and Ward A., to SPIE Journal of Medical Imaging, 2014 (in preparation).

1.6.2 Chapter 3: Evaluation of accuracy, inter-observer variability, and inter-sequence variability of tumour burden on multi-parametric MRI

Prostate tumour volume measurement can inform prognosis and treatment selection, including an assessment of the suitability and feasibility of focal therapy. MPMRI is showing promise for prostate cancer detection. We investigated the accuracy, inter-observer variability, and inter-sequence variability of tumour volume estimation via separate contouring of 3-Tesla T2W, DCE, and ADC images using a histologic reference standard. This chapter addresses objectives 5 and 6 as described in Section 1.5.

A version of this chapter has been published as "Accuracy and variability of tumour burden on multi-parametric MRI," by M. Salarian, M. Shahedi, E. Gibson, M. Gaed, J.A. Gomez, M. Moussa, G.S. Bauman, A.D. Ward, in the proceedings of SPIE Medical Imaging 2014.

1.6.3 Chapter 4: Summary and conclusion

This chapter summarizes the overall contributions and conclusions of this thesis.

1.6.4 Chapter 5: Future work

This chapter outlines some potentially productive areas of future work arising from this thesis.

1.7 References

1. *Canadian Cancer Statistics*, 2010, Canadian Cancer Society's steering committee: Toronto.

2. Karnik, V.V., *Evaluation of Registration in Support of 3D TRUS-Guided Prostate Biopsy*, in *Biomedical Engineering Graduate Program*2010, The University of Western Ontario.

3.   Gilbert Welch H., B.W.C., *Overdiagnosis in Cancer.* JNCI J Natl Cancer Inst, 2010. **102**(9): p. 605-613.

4.   Kelloff, G.J., P. Choyke, and D.S. Coffey, *Challenges in clinical prostate cancer: role of imaging.* AJR Am J Roentgenol, 2009. **192**(6): p. 1455-70.

5.   King, C.R., et al., *Extended prostate biopsy scheme improves reliability of Gleason grading: implications for radiotherapy patients.* Int J Radiat Oncol Biol Phys, 2004. **59**(2): p. 386-91.

6.   Turkbey, B., P.A. Pinto, and P.L. Choyke, *Imaging techniques for prostate cancer: implications for focal therapy.* Nat Rev Urol, 2009. **6**(4): p. 191-203.

7.   Burkhardt, J.H., et al., *Comparing the costs of radiation therapy and radical prostatectomy for the initial treatment of early-stage prostate cancer.* J Clin Oncol, 2002. **20**(12): p. 2869-75.

8.   Borofsky, M.S. and T. Ito, *Focal therapy for prostate cancer – where are we in 2011?* Therapeutic Advances in Urology, August 2011. **3**(4): p. 183-192.

9.   Ward, J.F. and J.W. Moul, *Rising prostate-specific antigen after primary prostate cancer therapy.* Nature clinical practice. Urology, 2005. **2**(4): p. 174-82.

10.   Egevad, L., J.R. Srigley, and B. Delahunt, *International Society of Urological Pathology (ISUP) consensus conference on handling and staging of radical prostatectomy specimens: rationale and organization.* Modern pathology : an official journal of the United States and Canadian Academy of Pathology, Inc, 2011. **24**(1): p. 1-5.

11.   Mouraviev, V., J.M. Mayes, and T.J. Polascik, *Pathologic basis of focal therapy for early-stage prostate cancer.* Nat Rev Urol, 2009. **6**(4): p. 205-15.

12.   Ward, A.D., et al., *Prostate: Registration of digital histopathologic images to in vivo MR images acquired by using endorectal receive coil.* Radiology, 2012. **263**(3): p. 856-864.

13.   Gibson, E., et al., *Registration of prostate histology images to ex vivo MR images via strand-shaped fiducials.* Journal of Magnetic Resonance Imaging, 2012. **36**(6): p. 1402-1412.

14.   E. Gibson, M.G., J. A. Gómez, M. Moussa, C. Romagnoli, M. Bastian-Jordan, Z. Kassam, D. W. Cool, S. Pautler, J. L. Chin, C. Crukley, G. S. Bauman, A. Fenster, A. D. Ward. *Toward prostate cancer contouring guidelines on MRI: dominant lesion gross and clinical target volume coverage via accurate histology fusion.* in *American Society for Radiation Oncology Annual Meeting*. 2014. San Diego, USA.

15.   Jim Clark, P.N., *WebMD*, 2009.

16.   *redorbit*. [cited 2002; http://www.redorbit.com/].

17.   McNeal, J.E., *The zonal anatomy of the prostate.* Prostate, 1981. **2**(1): p. 35-49.

18.   *Quizlet*. [http://quizlet.com/].

19.   *Wikimedia Commons.* [http://commons.wikimedia.org/].

20.   Jun Nakashimaa, et al., *Endorectal MRI for prediction of tumour site, tumour size, and local extension of prostate cancer.* Urology, July 2004. **64**(1): p. 101–105.

21.   McNeal, J.E., *The prostate and prostatic urethra: a morphologic synthesis.* J Urol, 1972. **107**(6): p. 1008-16.

22.   Ian M. Thompson, D.K.P., Phyllis J. Goodman, Catherine M. Tangen, M. Scott Lucia, Howard L. Parnes, Lori M. Minasian, Leslie G. Ford, Scott M. Lippman, E. David Crawford, John J. Crowley,Charles A. Coltman., *Prevalence of prostate cancer among men with a prostate-specific antigen level < or =4.0 ng per milliliter.* The New England Journal of Medicine, May 2004. **350**(22): p. 2239-2246.

23.   *Canadian Cancer Statistics*, 2013, National Cancer Institute.

24.   Schroder, F.H., et al., *Early detection of prostate cancer in 2007. Part 1: PSA and PSA kinetics.* Eur Urol, 2008. **53**(3): p. 468-77.

25.   Palmerola, R., et al., *The digital rectal examination (DRE) remains important - outcomes from a contemporary cohort of men undergoing an initial 12-18 core prostate needle biopsy.* Can J Urol, 2012. **19**(6): p. 6542-7.

26.   *gettyimages*. [cited 1999; http://www.gettyimages.ca/].

27.   Hodge, K.K., et al., *Random systematic versus directed ultrasound guided transrectal core biopsies of the prostate.* J Urol, 1989. **142**(1): p. 71-4; discussion 74-5.

28.   Fink, K.G., et al., *Evaluation of transition zone and lateral sextant biopsies for prostate cancer detection after initial sextant biopsy.* Urology, 2003. **61**(4): p. 748-53.

29.   Epstein, J.I., et al., *Utility of saturation biopsy to predict insignificant cancer at radical prostatectomy.* Urology, 2005. **66**(2): p. 356-60.

30.   Epstein, J.I., *Prognostic significance of tumour volume in radical prostatectomy and needle biopsy specimens.* J Urol, 2011. **186**(3): p. 790-7.

31.   Villeirs, G.M., et al., *A qualitative approach to combined magnetic resonance imaging and spectroscopy in the diagnosis of prostate cancer.* Eur J Radiol, 2010. **73**(2): p. 352-6.

32.   *ProstateHealthCures*. [http://www.prostatehealthcures.com/].

33.   Kattan, M.W., T.M. Wheeler, and P.T. Scardino, *Postoperative nomogram for disease recurrence after radical prostatectomy for prostate cancer.* J Clin Oncol, 1999. **17**(5): p. 1499-507.

34.   Hull, G.W., et al., *Cancer control with radical prostatectomy alone in 1,000 consecutive patients.* J Urol, 2002. **167**(2 Pt 1): p. 528-34.

35.   DeMarzo, A.M., et al., *Pathological and molecular aspects of prostate cancer.* Lancet, 2003. **361**(9361): p. 955-64.

36.   Epstein, J.I., *An update of the Gleason grading system.* J Urol, 2010. **183**(2): p. 433-440.

37.   Han, M., et al., *Long-term biochemical disease-free and cancer-specific survival following anatomic radical retropubic prostatectomy. The 15-year Johns Hopkins experience.* The Urologic clinics of North America, 2001. **28**(3): p. 555-65.

38.   Stamey, T.A., et al., *Morphometric and clinical studies on 68 consecutive radical prostatectomies.* J Urol, 1988. **139**(6): p. 1235-41.

39.   McNeal, J.E., et al., *Patterns of progression in prostate cancer.* Lancet, 1986. **1**(8472): p. 60-3.

40.   Ohori, M., et al., *Prognostic significance of positive surgical margins in radical prostatectomy specimens.* J Urol, 1995. **154**(5): p. 1818-24.

41.   Epstein JI, C.M., Partin AW, Walsh PC, *Is tumour volume an independent predictor of progression following radical prostatectomy? A multivariate analysis of 185 clinical stage B adenocarcinomas of the prostate with 5 years of followup.* The Journal of Urology 1993. **149**(6): p. 1478-1481.

42.   Salomon, L., et al., *Prognostic significance of tumour volume after radical prostatectomy: a multivariate analysis of pathological prognostic factors.* Eur Urol, 2003. **43**(1): p. 39-44.

43.   Stamey, T.A., et al., *Biological determinants of cancer progression in men with prostate cancer.* JAMA, 1999. **281**(15): p. 1395-400.

44.   Porten, S.P., M.R. Cooperberg, and P.R. Carroll, *The independent value of tumour volume in a contemporary cohort of men treated with radical prostatectomy for clinically localized disease.* BJU Int, 2010. **105**(4): p. 472-5.

45.   Tineke Woltersa, et al., *Should pathologists routinely report prostate tumour volume? The prognostic value of tumour volume in prostate cancer.* European Urology, May 2010. **57**(5): p. 821–829.

46.   van der Kwast, T.H., et al., *International Society of Urological Pathology (ISUP) Consensus Conference on Handling and Staging of Radical Prostatectomy Specimens. Working group 2: T2 substaging and prostate cancer volume.* Modern pathology : an official journal of the United States and Canadian Academy of Pathology, Inc, 2011. **24**(1): p. 16-25.

47.   Montironi, R., et al., *Handling and pathology reporting of radical prostatectomy specimens.* Eur Urol, 2003. **44**(6): p. 626-636.

48.   Rojo MG, G.G., Mateos CP, Garcia JG, Vicente MC *Critical Comparison of 31 Commercially Available Digital Slide Systems in Pathology.* International Journal of Surgical Pathology 2006. **14**(285-305).

49.   Treanor, D., et al., *Virtual reality Powerwall versus conventional microscope for viewing pathology slides: an experimental comparison.* Histopathology, 2009. **55**(3): p. 294-300.

50.   Turkbey B., M.H., Aras O., Rastinehad A.R., Shah V., Bernardo M., Pohida T., Daar D., Benjamin C., Mckinney Y.L., Linehan W.M., Wood B.J., Merino M.J., Choyke P.L., and Pinto P.A. , *Correlation of Magnetic Resonance Imaging Tumour Volume with Histopatology.* The Journal of Urology, 2012. **188**: p. 1157-1163.

51.   Kitajima, K., et al., *Prostate cancer detection with 3 T MRI: comparison of diffusion-weighted imaging and dynamic contrast-enhanced MRI in combination with T2-weighted imaging.* J Magn Reson Imaging, 2010. **31**(3): p. 625-31.

52.   Kiajima K., K.Y., Fukabori Y., Yoshida K., Suganuma N., and Sugimura K. , *Prostate Cancer Detection With 3T MRI: Comparison of Diffusion-Weighted Imaging and Dynamic Contrast-Enhanced MRI in Combination With T2-*

Weighted Imaging. Journal of Magnetic Resonance Imaging, 2010. **31**: p. 625-631.

53.   Barentsz J.O., R.J., Clements R., Choyke P., Verma S., Villeirs G., Rouviere O., Logager V., and Futterer J.J, *ESUR prostate MR guidlines 2012.* Eur Radiol, 2012. **22**: p. 746-757.

54.   Alonzi, R., A.R. Padhani, and C. Allen, *Dynamic contrast enhanced MRI in prostate cancer.* Eur J Radiol, 2007. **63**(3): p. 335-50.

55.   Tan, C.H., J. Wang, and V. Kundra, *Diffusion weighted imaging in prostate cancer.* Eur Radiol, 2011. **21**(3): p. 593-603.

56.   Magi-Galluzzi, C., et al., *International Society of Urological Pathology (ISUP) Consensus Conference on Handling and Staging of Radical Prostatectomy Specimens. Working group 3: extraprostatic extension, lymphovascular invasion and locally advanced disease.* Modern pathology : an official journal of the United States and Canadian Academy of Pathology, Inc, 2011. **24**(1): p. 26-38.

57.   Masanori Noguchi, et al., *Assessment of Morphometric Measurement of Prostate Carcinoma Volume.* American Cancer Society, September 2000. **89**(5): p. 1056–1064.

58.   Chen, M.E., et al., *A streamlined three-dimensional volume estimation method accurately classifies prostate tumours by volume.* Am J Surg Pathol, 2003. **27**(10): p. 1291-301.

59.   Haffner J, P.E., Bouyé S, Puech P, Leroy X, Lemaitre L, Villers A, *Peripheral zone prostate cancers: location and intraprostatic patterns of spread at histopathology. .* The Prostate, Feburary 2009. **69**(3): p. 276-82.

60.   Osher, S. and J.A. Sethian, *Fronts propagating with curvature-dependent speed: Algorithms based on Hamilton-Jacobi formulations.* J Comp Phys, 1988. **79**: p. 12-49.

61.	Coakley F.V., K.J., Lu Y., Jones K.D., Swanson M.G., Chang S.D., Carroll P.R., and Hricak H., *Prostate Cancer Tumour Volume: Measurement with Endorectal MR and MR Spectroscopic Imaging.* Radiology, 2002. **223**: p. 91-97.

Chapter 2

2 Toward quantitative digital histopathology for prostate cancer: comparison of inter-slide interpolation methods for tumour measurement

2.1 Introduction

Prostate cancer (PCa) is the most common non-cutaneous cancer among men, with hundreds of thousands of diagnoses and tens of thousands of deaths annually [1]. In 2012, it was the second leading cause of cancer death among North American men, with an estimated 268,240 diagnoses and 32,170 deaths [2]. Approximately 40% of men with organ-confined PCa undergo radical prostatectomy (surgical removal of the entire prostate), with nearly 80,000 surgeries per year in the United States [3]. After surgery, about 35% of patients have subsequent biochemical failure (BCF) [4], which is measured by an increase in prostate-specific antigen (PSA) in the blood, with increased risk of metastatic cancer and death [5]. After BCF, it may be possible to cure the patient by applying follow-up curative-intent androgen deprivation [6], or prostate bed irradiation [7] to destroy any remaining cancer. Pre-emptive (adjuvant) follow-up therapy has been shown in clinical trials to improve cancer control and reduce BCF [7]. However, the clinical decision of whether to apply adjuvant therapy is important and challenging. Adjuvant therapy cannot be used for all patients due to the serious side effects that can occur, but can be life-saving for appropriate patients. *Identification of prostatectomy patients who are at elevated risk of biochemical failure and would benefit from post-prostatectomy adjuvant therapy is therefore critical to PCa control and cure.*

The pathologist's assessment of the removed prostate is very important to this clinical decision [8]. Traditional surgical pathology assessment of prostatectomy specimens includes tissue fixation in buffered formalin for 12–48 hours followed by

slicing into 3–5 mm thick tissue sections which are subsequently embedded in paraffin blocks. Tissue sections 4–5 µm in thickness are then cut with a microtome from each block face for hæmatoxylin and eosin (H&E) staining. The pathologist then conducts a microscopic examination of the sections. Each tumour is assessed in several ways, including (but not limited to) location within the prostate, volume assessment and degree of differentiation (the latter using the Gleason grading system [9]). *The determination of whether a patient is a candidate for adjuvant therapy depends in part on prognostic information derived from the total volumes and Gleason grades of the tumours assessed on the resected specimen [8].*

Tumour volume assessment in the radical prostatectomy specimen is particularly challenging to report quantitatively, and substantial variability has been reported in the volume estimation methods used clinically [10, 11]. The ongoing transition to digital pathology has been fostered by high-resolution whole-slide scanners and opens the possibility for the integration of computational tools into the digital pathology workflow in order to enable quantitative assessments and reporting in a clinically feasible fashion. The emergence of automatic techniques for prostate cancer detection and localization on 2D digital pathology imaging [12-14] provides an opportunity for computer-assisted tumour quantification. However, clinicians interpreting pathology reports require an understanding of the 3D tumour burden when making treatment decisions. One important challenge to 3D tumour volume quantification is the sparse sampling of the prostate tissue performed during the usual clinical pathology protocol [15]. For reasons of practicality and cost, 4 µm tissue sections are typically obtained at 3–5 mm intervals for mounting on microscope slides (this interval is henceforth referred to as *inter-slide* spacing) for clinical prostate specimens. Thus, in 3D, digital pathology imaging of clinical prostate specimens contains much denser information within each slide (often 0.25–0.50 µm pixels), relative to the information obtained in the through-slide direction.

In the current absence of widespread clinical implementation of whole slide scanning and automated tumour delineation, there are several simpler approximations to prostate tumour volume measurement that have been used clinically and in the research setting. Examples include measurement of the diameter of the largest tumour focus,

assessment of maximum tumour area using a single or multiple slide approach, counting of the number of involved blocks, assessment of the positive to negative block ratio, use of a measuring grid, and point counting [16, 17]. To evaluate these approaches, a planimetric method has been used in several studies as a reference standard for estimating tumour volume on digital pathology of the prostate [16, 18, 19]. In this method, each tumour is contoured on each slide, and tumour volume is calculated by multiplying the estimated within-slide tumour area by the inter-slide spacing. This approach will henceforth be referred to as the *nearest-neighbour* (NN) interpolation method, since the tumour shape on any parallel plane between two sections is estimated to be the same as the tumour shape on its nearest neigbouring section. This method has the advantage of being relatively straightforward from a computational standpoint. However, due to the large difference between the slice thickness (4–5 µm) and slide spacing (3–5 mm), this approach can produce sharp changes in the tumour surface along the direction orthogonal to the slides, bringing the biological plausibility of the 3D interpolation into question. This concern may be mitigated by a through-slide tumour boundary interpolation method designed to produce smooth tumour surfaces. In this work, we implemented and tested a *level set* (LS)-based interpolation scheme for this purpose, on which we provided a preliminary report in a conference proceedings [20]. This chapter extends our previous work in several important ways. Specifically, in this chapter, we measured the accuracy of the LS method for tumour boundary interpolation in comparison to the NN method, and measured the suitability of simpler tumour volume estimation techniques as surrogates for the tumour volumes calculated from the smooth tumour surfaces given by the LS method. As a secondary question, we examined the effect of modifying inter-slide spacing on the variability of tumour volume estimates, as this can inform optimization of pathology protocols for reproducibility of tumour volume estimation. With the clinical transition to whole-slide digitization and automated analysis on the horizon, the knowledge generated by this work can inform the choice of tumour volume measurement approach that provides the most appropriate balance of accuracy versus efficiency in the clinical pathology environment.

2.2 Materials and Methods

2.2.1 Materials

In this study, we acquired images from two different cohorts of patients, to support the evaluation of our tested tumour volume measurement methods in two ways. Both cohorts are part of clinical trials currently underway at our centre, both approved by the human subject research ethics board of our institution with written informed consent obtained from all patients. One cohort is a set of radical prostatectomy patients for whom we have 2D tumour contours on post-prostatectomy histology. The other cohort is a set of patients who underwent magnetic resonance imaging (MRI)-targeted, 3D transrectal ultrasound-guided "fusion" prostate biopsy, for whom we have 3D tumour contours on pre-biopsy MRI. The specific details of each cohort are described in the following subsections.

2.2.1.1 Radical prostatectomy patients

Twenty-one patients with biopsy-proven prostate cancer who underwent radical prostatectomy between June, 2010 and December, 2011 were recruited by three collaborating urologists/surgical oncologists. The inclusion criteria were: (1) age 18 years or older, (2) clinical stage T1 or T2 prostate cancer histologically confirmed by biopsy, and (3) suitable for and consenting to radical prostatectomy. The exclusion criteria were: (1) prior therapy for prostate cancer, (2) use of 5-alpha reductase inhibitors within 6 months of the study start, (3) inability to comply with preoperative imaging, (4) allergy to contrast agents, (5) sickle cell or other anemias, (6) hip prosthesis, (7) sources of artifact within the pelvis, and (8) contraindications to MRI.
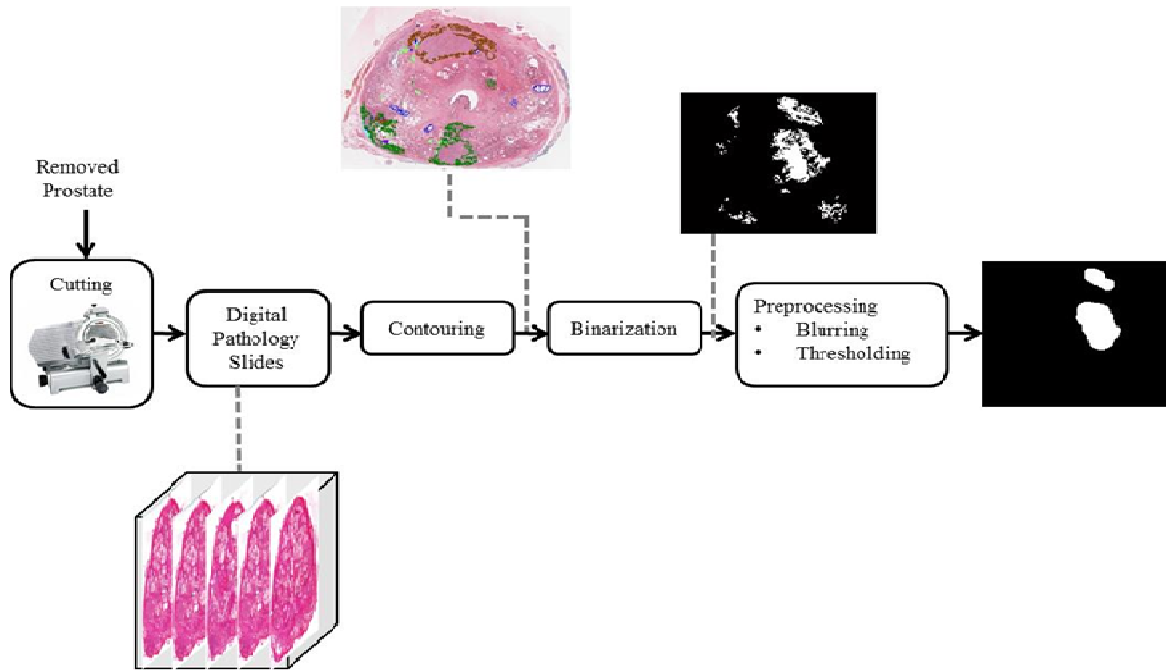
Figure 2.1. Block diagram describing the data acquisition and pre-processing from our radical prostatectomy patients.

The schematic in Figure 2.1 provides a high level description of the data acquisition and pre-processing we performed for the radical prostatectomy patients. The details from radical prostatectomy up to and including image preprocessing are as follows. For each patient, after radical prostatectomy, the resected prostate was fixed in 10% buffered formalin for 48 hours. Each specimen was then transversely sliced into 4.4 mm thick tissue slices, which were paraffin-embedded. A single 4 μm-thick whole-mount hæmatoxylin and eosin-stained tissue section was taken from each block face and mounted on a positively-charged glass slide. The slides were digitized using a ScanScope GL (Aperio Technologies, Vista, CA, USA) bright field slide scanner. The acquired images were 24-bit colour with isotropic 0.5 μm^2 pixels. From each patient, between 3 and 5 (median 4) whole-mount sections were obtained; 82 such sections were obtained in total. For each specimen, adjacent section images were aligned using orientation

information derived from our previously developed method for 3D histology reconstruction [21].

An experienced clinician contoured and graded all lesions on each histology image using the ScanScope ImageScope v11.0.2.725 software (Aperio Technologies, Vista, CA, USA) and a Cintiq pen-enabled display (Wacom Co. Ltd., Saitama, Japan); these contours were reviewed and edited as necessary by one of two genitourinary pathologists. We designated all tumour areas containing any Gleason grade 4 or 5 as high-grade; all other tumours were designated as low-grade. Figure 2.2 shows an illustrative example of this contouring; note the variability of tumour shapes in Figure 2.2(a-d). Contouring was performed at high magnification (i.e. using the 20× magnification setting in the ImageScope software (Figure 2.2(f)), rendering 0.5 µm × 0.5 µm pixels). Figure 2.2(e) and (f) provide an illustration of the attention to detail applied to this contouring task. From these contours, we extracted a total of 144 tumours, 110 of which were low-grade (from all 21 patients) and 34 of which were high-grade (from 16 patients). 126 tumours spanned a single microscope slide, 14 tumours spanned 2 slides, 3 tumours spanned 3 slides, and 1 tumour spanned 4 slides. For improved processing speed and to close small gaps introduced by the meticulous contouring (Figure 2.2(f)), each slide was rasterized to a 0.25 mm × 0.25 mm pixel binary image and thresholded at 0.5 after preprocessing using a 1 mm-radius disk-shaped averaging filter.
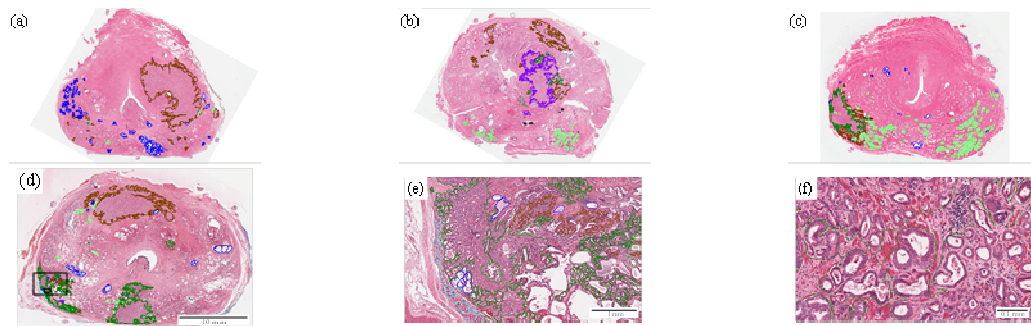
Figure 2.2. (a-d) Sample contoured whole-mount histopathology images. **(e)** and **(f)** are zoomed from the large and small boxes in **(d)**, respectively. Colour code is as follows. Brown: low-grade cancer. Gray, dark green, purple: regions containing several different grades of cancer, all including some high-grade cancer. Cyan: extraprostatic extension of tumour. Blue: atrophy (benign). Light green: prostatic intraepithelial neoplasia (benign).

2.2.1.2 MRI-targeted fusion biopsy patients

Fourteen patients underwent prostate MPMRI using a Discovery MR750 (GE Healthcare, Waukesha, WI, USA) at 3T using T2W, T1-weighted dynamic contrast-enhanced, and diffusion-weighted sequences (sequence parameters shown in Table 2.1). Pelvic phased array and endorectal receive coils were used simultaneously for these acquisitions. The schematic in Figure 2.3 provides a high level description of the data acquisition and pre-processing we performed for the radical prostatectomy patients. After MPMRI acquisition, a radiologist and radiology resident, each with > 5 years of experience reading > 200 prostate MRI cases, assessed the multi-parametric MRI using guidelines concordant with the prostate imaging and reporting data system (PI-RADS) [12] and delineated a total of 24 3D tumour volumes on the MRI. All three sequences were used to identify tumours (as in the PI-RADS guidelines), and the tumours were contoured in the coordinate system of the T2W images. These contours were performed using custom software that allowed the operator to manipulate control points defining a 3D tumour surface with subvoxel precision. This approach mitigates segmentation precision issues arising due to the thickness of the MR image planes. This yielded 14 3D label maps in the T2W coordinate system, one for each patient, depicting a total of 24 contoured tumour regions. For each of the 3D contoured tumours, we calculated tumour volume by multiplying the number of voxels within each region by the voxel size in mm^3.

Table 2.1. MRI sequence parameters.

Sequence	T2W	DCE	DW
Repetition time (msec)	4833	3.1	4000
Echo time (msec)	160	1.5	70–77
Bandwidth (kHz)	31.25	83.33	166.7
Number of excitations	4	1	3
Field of view (cm)	14	14	14
Slice thickness (mm)	2.2	3.0	3.6
Slice spacing (mm)	0	0	0
Matrix	320×192	128×128	128×256
Number of slices	30-40	32	20–34
Flip angle (°)	90	12	90
Temporal spacing (s)	N/A	6-7	N/A
B-value	N/A	N/A	100, 800
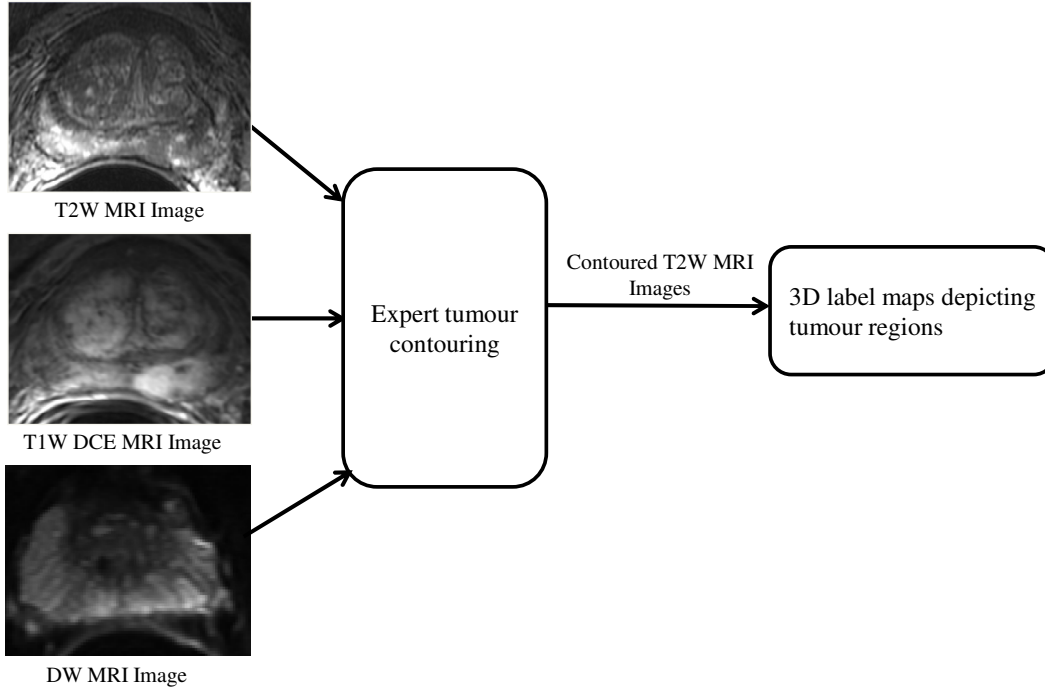
Figure 2.3. Block diagram describing the data acquisition and pre-processing from our fusion biopsy patients.

2.3   Methods

In this section, we describe the level set-based tumour interpolation method we developed, a set of conventional methods that have been previously reported in the literature, and our approaches to measurement of tumour volume accuracy. All data processing in this work was performed using custom software written in Matlab 7.12.0 (The Mathworks, Inc., Natick, MA, USA).

2.3.1 Level set-based interpolation method for tumour volume estimation

We implemented an approach to shape interpolation that is based on the level set representation (as distinct from the often-reported use of the level set representation for image segmentation) [22]. Our rationale for the use of a level set based approach is based on our observation that histologic tumour shapes are complex and can change in topology from one slide to the next (e.g. a 3D tumour can appear as a single connected 2D component on one slide and multiple disconnected 2D components on an adjacent slide).

The level set representation is ideally suited for such shape interpolation problems. The level set implicitly represents shape boundaries using a signed distance map defined everywhere in the image domain, where zero crossings define the shape boundaries. Through-slide interpolation of these signed distance values produces a smooth evolution of complex boundary shapes from one slide to the next.
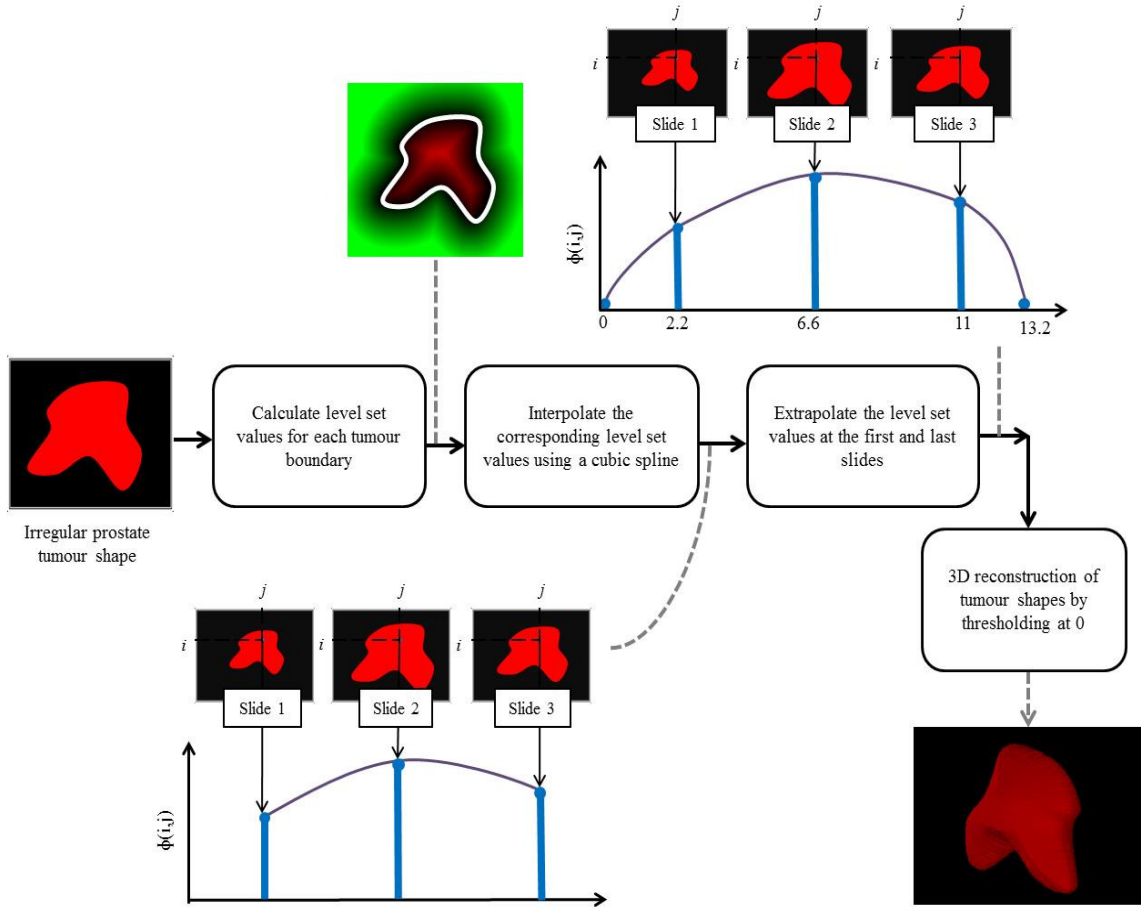
Figure 2.4. Block diagram describing the steps involved in the level set-based interpolation method.

Figure 2.4 provides a schematic showing the steps of our LS-based shape interpolation method. On each slide, we represent the tumour cross section as a 2D binary image, with pixels covering an area of 0.25 mm × 0.25 mm. For each such image $I(i,j): \mathbb{Z}^2 \rightarrow \{0,1\}$ a level set representation $\varphi(i,j): \mathbb{Z}^2 \rightarrow \mathbb{R}$ was calculated by computing the signed distance transformation of the shape boundary. To interpolate

tumour shapes between slides having an inter-slide spacing of s mm (s = 4.4 in our study), pixel correspondence was established according to (i, j), and corresponding level set values $\varphi(i, j)$ were interpolated in increments of t mm in the through-slide direction using a cubic spline. In our study, we set t to 0.2 mm; thus, our tumours were interpolated in a 3D coordinate system with 0.25 mm × 0.25 mm × 0.2 mm voxel size. To avoid flat "caps" of the tumours at the first and last slides, we defined extrapolated level sets at $s/2$ mm from each cap via level set evolution using speed a function that was constant throughout the domain (i, j). The constant was chosen such that the evolving level set would cause the shape to vanish at $min(r, s/2)$ mm from the first and last slides of the tumour, where r was defined as $max(\varphi(i, j))$. This choice of speed function encourages 3D isotropy of one-slice tumours and guarantees that tumours will not be extrapolated into regions where they are known not to exist (based on their absence from adjacent contoured slides). The extrapolated level sets were incorporated into the spline interpolation as described above. Thus, 1-slide tumours were interpolated using 3 level sets, 2-slide tumours using 4 level sets, etc. After interpolation, the final 3D shapes were defined by thresholding the interpolated level sets at 0, yielding a 3D binary image containing each tumour. Tumour volume was calculated as the number of voxels within the tumour region multiplied by the voxel size.

2.3.2 Conventional tumour size estimation methods

To compare the LS-based volume estimation approach with previously-defined approaches, we performed several tumour volume estimation calculations as described in [16, 19] and enumerated as follows. (1) In the *nearest-neighbour (NN)* planimetric approach, tumour volume was calculated by multiplying the area within each contoured tumour on each slide by the inter-slide spacing, and summing these areas for tumours appearing on multiple slides. Thus, this approach requires that the entire tumour be outlined on every slide on which it appears. (2) In the *maximum tumour diameter (MTD)* approach, tumour size was estimated as the length of the longest chord within the tumour on any of the slides on which it appeared. Thus, this method is considerably less labour-intensive, requiring only that the pathologist find the slide containing the largest tumour cross section and take a single linear measurement. (3) In the *estimated square area*

(ESA) approach, tumour size is estimated by multiplying the MTD by the length of the longest chord perpendicular to the chord used to calculate MTD; effectively this is the area of a bounding box of the largest tumour cross section. This method is also much less labour intensive than the NN approach, requiring only two linear measurements on a single slide. (4) In the *cubic volume (CV)* approach, tumour volume was estimated as the product of ESA and the total cross-sectional thickness of the tumour (i.e. the number of slides on which the tumour appeared, multiplied by the inter-slide spacing).

2.3.3 Tumour volume accuracy measurement and comparison

An ideal means for measuring the accuracy of 3D tumour volume measurement on histology would be to perform a complete serial step sectioning of the prostate tissue, perform expert manual contouring of the tumours on each section, and calculate tumour volume as the sum of cross sectional tumour areas, multiplied by the section thickness (e.g. 4 µm). However, this approach is impractical for two primary reasons. First, for a prostate measuring 4 cm in the inferior-superior direction orthogonal to the plane of sectioning (a typical size of a radical prostatectomy specimen), complete serial sectioning at 4 µm would yield 10,000 sections to be mounted on slides, stained, coverslipped, scanned, and processed. This is clearly a cost-prohibitive process to perform for any reasonable number of specimens in a study, and to the best of our knowledge, only a single specimen has been processed in a similar fashion and reported in the literature [23]. Second, clinical pathology departments require that most of the tissue from radical prostatectomy specimens be retained in paraffin blocks to aid in diagnosis of future malignancies in the patient. Consequently, from clinical specimens, one obtains a thin tissue section at widely spaced intervals throughout the prostate (typically 3–5 mm in clinical practice); in our study, we obtained a section every 4.4 mm. Thus, practical and cost considerations aside, regulations dictate that complete serial sectioning of prostates could be performed only on autopsy specimens, where inclusion and exclusion criteria may be more challenging to measure. Thus, surrogates for this ideal reference standard for histologic tumour volume are valuable to the evaluation of tumour volume estimation algorithms.

We used two different reference standards to evaluate the LS and NN interpolation methods. Our first reference standard is the set of 3D tumour shapes contoured on multiparametric MRI from our fusion biopsy cohort. We simulated histologic sectioning of these shapes by extracting 2D cross sections at specified spacing, and then measured the accuracy of the different interpolation methods in reconstructing the original 3D shapes. This reference standard has the advantage of being inherently 3D, but has the disadvantage of consisting of a set of shapes that are not directly derived from a histologic assessment of the tumours. The shapes are indirectly measured on MRI and thus we consider them to be plausible, not actual, tumour shapes. As a complementary approach to address this issue, our second reference standard is the set of 2D tumour contours on histology images from our radical prostatectomy cohort. To test the interpolation methods using this reference standard, we drop one dimension from the interpolation calculations. That is, rather than interpolating 2D cross sections to a 3D shape, we use the same interpolation methods to interpolate 1D cross sections a 2D shape; we can then use the 2D histologic contours as a reference standard. Although this reference standard has the disadvantage of being intrinsically 2D, it has the advantage of being measured directly from the histologic images, consisting of actual tumour shapes, and is thus complementary to our MRI-based reference standard.

We tested the performance of the tumour size estimation methods under idealized tumour slicing conditions, where the set of slices were centered within the tumour, and the distance between the outermost slices and the true tumour edges was known (Figure 2.5(a)). This idealized arrangement is not generally obtained in practice, but serves as a means for a baseline comparison of the best-case performances of the methods. More specifically, our assumption was that the tumours were cut with a T mm spacing (we used $T = 4.4$ mm, as this is the spacing used in our radical prostatectomy cohort) between slides, and that the distance X (mm) between the outermost slides and the ends of the tumour were known. This is described in the diagram in Figure 2.5(a). As a further illustration in the context of the 3D MRI-based reference standard, consider a tumour with *length* L mm (henceforth taken to be the tumour size measured in the direction orthogonal to the slides) less than T mm. To provide the interpolation algorithms with a

simulated histologic tumour cross section, a cross sectional slice from the MRI must be selected. In this idealized experiment, the selected slice was at the midpoint between the tumour extents, and $X = L/2$ mm. For a tumour with L > T, s > 1 MRI slices were selected such that the outermost slices are equidistant from the ends of the tumour, and $X = (L - T \times (s - 1))/2$ mm. For the 2D histology-based reference standard, the calculations were the same, except that rather than extracting 2D cross sections from the 3D contoured MR images, instead we extracted 1D cross sections from the 2D contoured histology images.

2.3.4 Assessment of impact of inter-slide spacing on variability of tumour volume estimation

Since tumour volume on histology must be measured using sparsely sampled 2D histology sections, the estimated volume depends in part on the spatial locations where the cuts are made in the specimen to take the sections. Thus, the estimated volume may vary as a function of the positioning of these cuts; this variability may be mitigated by taking a larger number of more closely-spaced sections. The choice of inter-slide spacing involves a compromise between the benefits of increased sampling of the specimen (smaller spacing), and benefits of reduced time and costs with fewer slides (larger spacing). Using our MRI-based 3D reference standard, we measured the effect of varying inter-slide spacing on volume estimation by computer simulation. We simulated slicing at all possible knife blade positions within the specimen (quantized to 0.2 mm steps) with the inter-slide spacing values ranging from 2 mm to 6 mm, in 1 mm increments. For each spacing, we measured the standard deviation of the tumour volume estimates across all blade positions, for both the LS and NN methods.

To assess the impact of inter-slide spacing on variability of tumour volume estimation, we fully relaxed the assumption of ideal slicing, and simulated all possible spatial arrangements of slices within the tumour (Figure 2.5(b)). This experiment provides results closer to what would be expected if the methods were put into use in a clinical environment, where the tumours within the prostate are not visible to the histotechnologist during the slicing process, and therefore the histotechnologist has no

means of controlling the slicing for optimal sampling of the tumours. More specifically, this experiment relaxed the assumption of ideal tumour slicing by testing the interpolation approaches through all possible slicing configurations (quantized to 0.2 mm steps). In addition, knowledge of the tumour extents beyond the outermost slices was not assumed; the locations of these extents were estimated to be $T/2$ mm beyond the outermost slices. This is described in the diagram in Figure 2.5(b). As a further illustration in the context of the 3D MRI-based reference standard, consider a tumour with *length* $L < T$ mm. To provide the interpolation algorithms with a simulated histologic tumour cross section, a cross sectional slice from the MRI must be selected. In this experiment, we repeated the interpolation for every cross sectional slice, in 0.2 mm increments, throughout the length of the tumour. For a tumour with L > T, s > 1 MRI slices were selected repeatedly for every possible positioning of such evenly spaced slices (T mm spacing) within the tumour. In all cases, the surface was extrapolated to $T/2$ mm extents on either side of the outermost extracted slice(s). For the 2D histology-based reference standard, the calculations were the same, except that rather than extracting 2D cross sections from the 3D contoured MR images, instead we extracted 1D cross sections from the 2D contoured histology images.
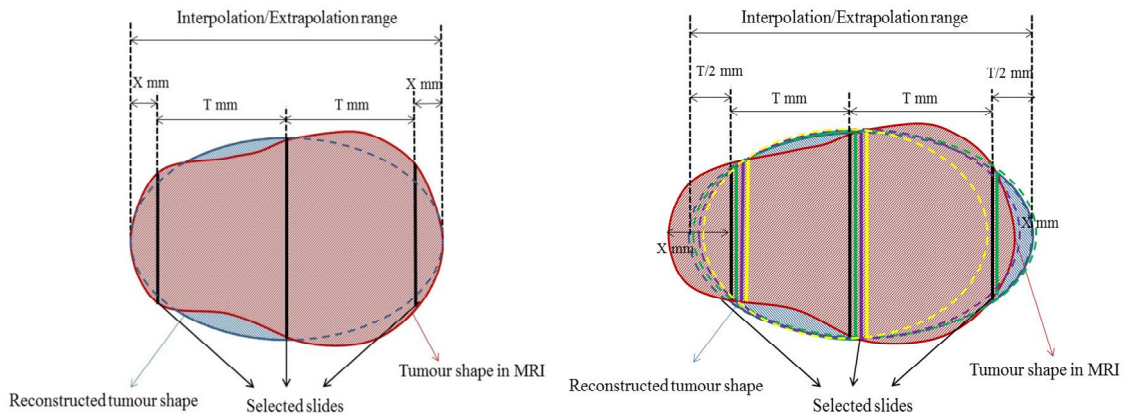
Figure 2.5. (a) Depiction of slice positions and extrapolation regions for experiments simulating idealized slicing. **(b)** Depiction of slice positions and extrapolation regions for experiments simulating realistic slicing. For clarity, only four possible slicing

configurations are shown (black, green, purple, and yellow) but in the experiments, all possible slicing configurations are used.
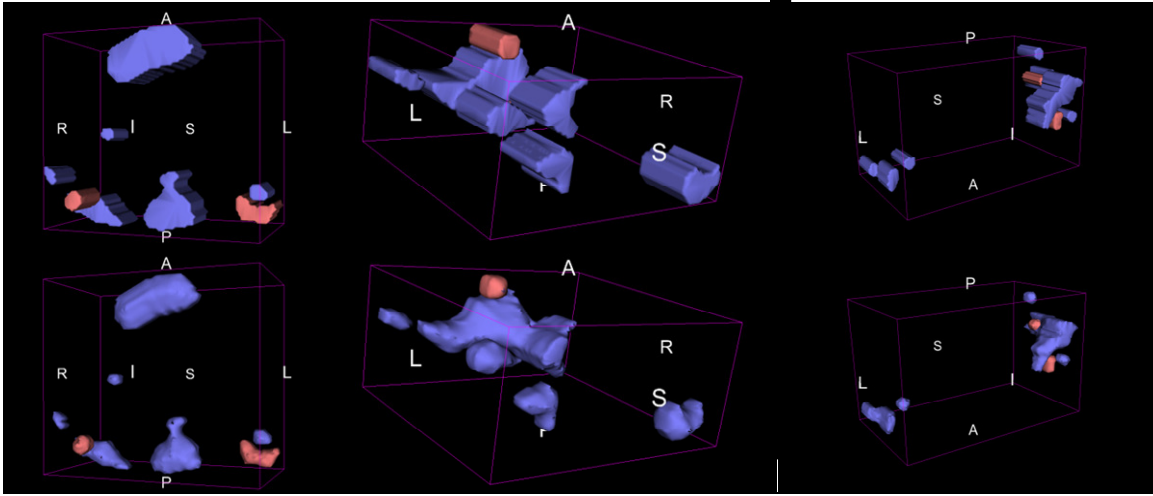
Figure 2.6. 3D surface renderings of interpolated tumours for three patients (one per column), under idealized tumour slicing assumptions. Low grade tumours are in blue and high grade tumours are in red. **Top row:** NN interpolation approach. **Bottom row:** LS-based interpolation approach.

2.4   Results

2.4.1   Tumour volume accuracy measurement and comparison

Figure 2.6 illustrates qualitative results of 3D tumour shape interpolation for 3 patients, showing 3D surface renderings of interpolated tumours using the NN interpolation and LS-based interpolation approaches using 3D Slicer version 3.6 (Surgical Planning Lab, Harvard Medical School, Boston, USA) [24]. Low-grade tumours are shown in blue and high-grade tumours are shown in red. Notable is the increased plausibility of the 3D tumour shapes produced via the LS-based interpolation approach. These 3D interpolations are comparable to our MRI-based reference standard for accuracy assessment. Figure 2.7 provides a similar illustration of the qualitative results in 2D, which are comparable to our histology-based reference standard for accuracy assessment. In this figure, the true histologic boundaries are shown overlaid

with the interpolated boundaries; note the superior agreement of the LS-based boundaries to the reference boundaries.
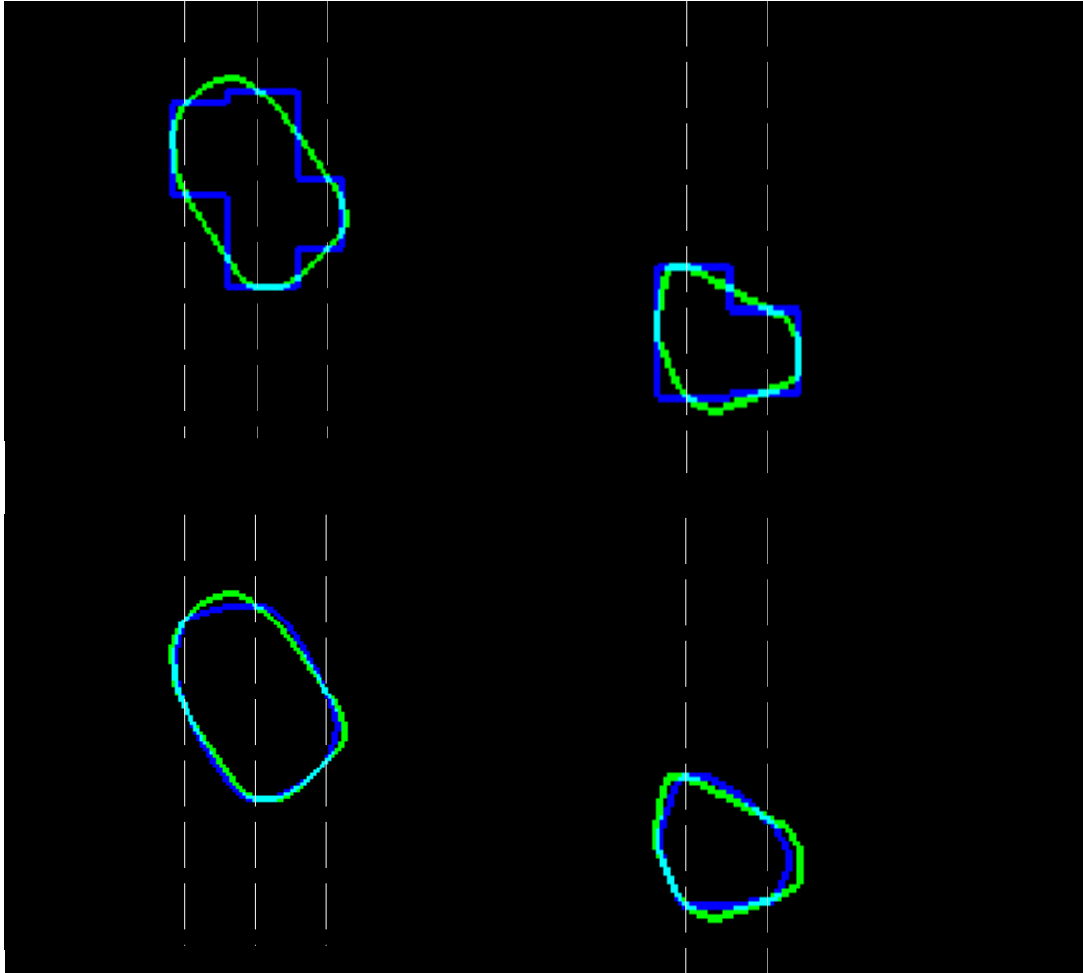
Figure 2.7. 2D boundaries of interpolated tumours for two patients (one per column), with the true boundaries from the contoured histology in green and the interpolated boundaries in blue, under idealized tumour slicing assumptions. The dashed lines show the 1D sampling regions from which the interpolations were performed. **Top row:** NN interpolation approach. **Bottom row:** LS-based interpolation approach.

Table 2.2 shows descriptive statistics for the volume estimates given by the NN and LS approaches, with breakdown according to high-grade vs. low-grade tumours, and breakdown according to whether the tumours occupied a single slide (i.e. cases where $L < T$) vs. cases where the tumours occupied more than one slide. We performed one-

sample Kolmogorov-Smirnov normality tests of the tumour volumes computed using the two methods. Our data did not pass the normality tests, necessitating the use of non-parametric hypothesis tests. We used both the Wilcoxon sign rank test and the Mann-Whitney U-test to test the null hypothesis that the median volume measured by the NN method was the same as that measured by the LS method. The null hypothesis was rejected by both tests ($p < 0.001$). Thus, the NN interpolation approach produces a larger tumour volume compared to the LS-based interpolation approach by a median factor of 2.3 overall.

Table 2.2. Descriptive statistics of tumour volumes estimated based on histologic tumour contours by the NN and LS methods for the radical prostatectomy patients.

Tumours	Interpolation	Tumour volume (mm^3)			
		Mean	Std. dev.	Median	IQR
All	NN	38.1	81.2	13.2	15.6
	LS	23.9	65.5	5.7	7.5
Low-grade	NN	37.7	59.4	14.1	22.1
	LS	23.2	47.4	6.1	11.1
High-grade	NN	40.1	141.7	12.4	2.2
	LS	26.8	115	5.3	1.1
1-slide	NN	21.8	24.2	13.2	8.8
	LS	10.5	14.5	5.6	3.9
>1-slide	NN	174.9	194	111.4	152.1
	LS	135.7	159.9	89.6	123.3

The scatter plots in Figure 2.8 depict the relationships between the volumes measured using the NN and LS approaches, for the radical prostatectomy patients and the fusion biopsy patients. For the radical prostatectomy patients (Figure 2.8(a)), we found different linear relationships between the volumes for 1-slide tumours (blue points) and >1-slide tumours (red points), with correlation coefficient $r = 0.99$ for both. We used linear regression ($LS\ Volume = a(NN\ Volume) + b$) to elucidate the relationships; the coefficients are shown in the tables within the figure. After using these linear models to adjust the NN-based volumes, the Bland-Altman plots in Figure 2.9 depict the residual differences between the two methods. These plots indicate negligible bias, with tighter limits of agreement for the radical prostatectomy cohort. This suggests that the

difference in volume estimates for the two methods is larger for larger tumours, as seen in the fusion biopsy cohort.
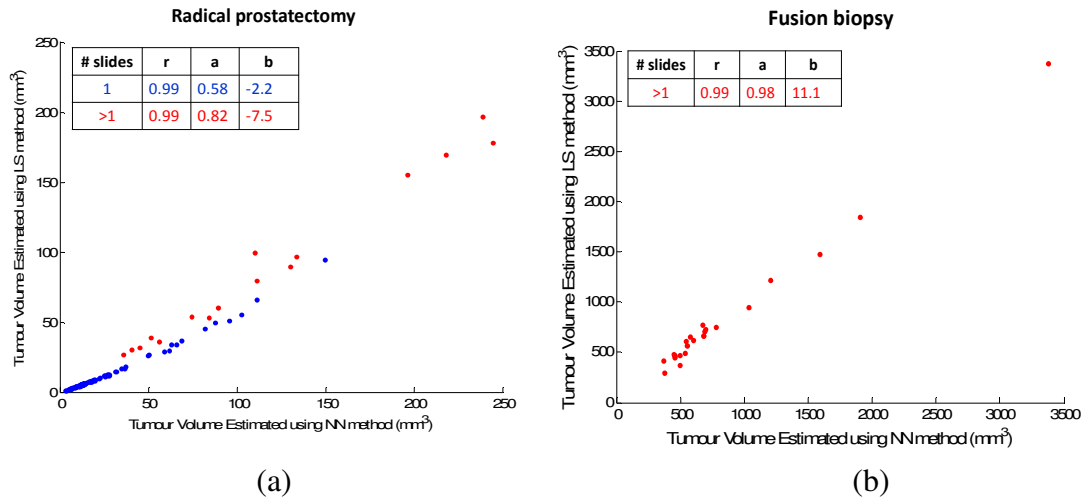
Figure 2.8. Comparison of volumes estimated using the NN and LS-based interpolation methods on **(a)** the radical prostatectomy patients and **(b)** the fusion biopsy patients, under idealized tumour slicing assumptions. Blue points: 1-slide tumours. Red points: >1-slide tumours. For clarity of interpretation, two high-volume outliers (high-grade tumours with level set volumes of 480 mm^3 and 824 mm^3) were omitted from (a).
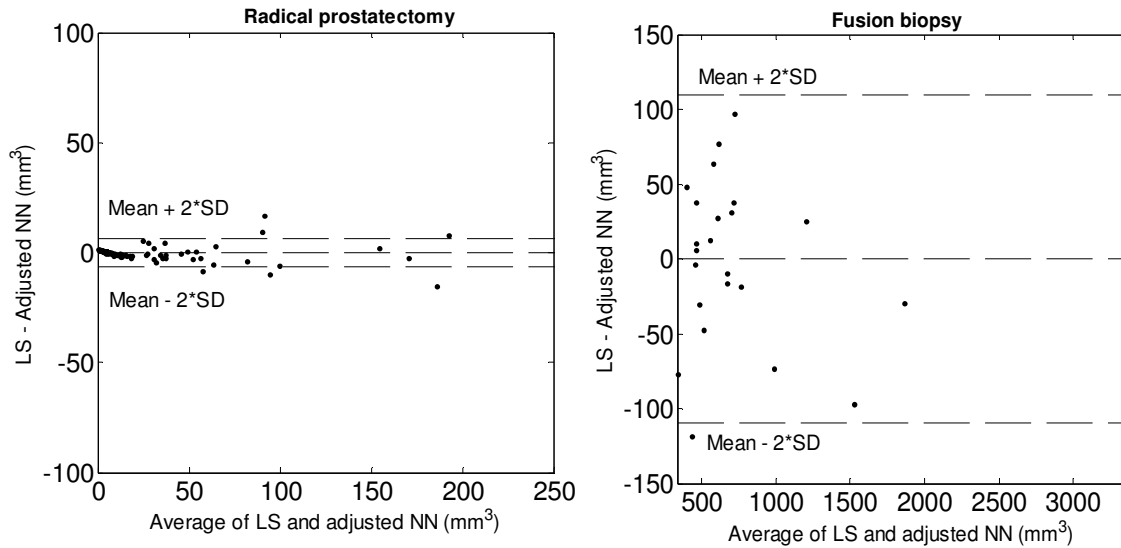
Figure 2.9. Bland-Altman plots for **(a)** the radical prostatectomy patients and **(b)** the fusion biopsy patients, under idealized tumour slicing assumptions. For clarity of interpretation, two high-volume outliers (high-grade tumours with level set volumes of 480 mm^3 and 824 mm^3) were omitted from (a).

The scatter plots in Figure 2.10 depict the relationships between the tumour sizes measured using the simpler MTD, ESA, and CV approaches, and the NN and LS approaches. For the relationships involving cubic volume, a linear regression was used, with coefficients shown in the tables within the figures. As MTD and ESA are measured in mm and mm^2 units, respectively, their relationships to the NN and LS tumour volumes measured in mm^3 units were elucidated by fitting cubic and quadratic polynomials, respectively, with coefficients shown. The cubic polynomial has the form $LS\ Volume = a \times (NN\ Volume)^3 + b \times (NN\ Volume)^2 + c \times (NN\ Volume) + d$. The quadratic polynomial has the form $LS\ Volume = a \times (NN\ Volume)^2 + b \times (NN\ Volume) + c$. The scatter plots and coefficients indicate that different relationships exist for 1-slide and >1-slide tumours. After using these models to adjust the MTD, ESA, and CV-based size estimates, the Bland-Altman plots in Figure 2.11 depict the residual differences between these methods and the NN and LS-based methods. One can observe that the relationships between the tumour sizes estimated

43

using the simpler approaches and the LS and NN approaches are similar, and the limits of agreement become smaller as one moves from the one-dimensional MTD size estimate to the two- and three-dimensional ESA and CV approaches.

Maximum tumour diameter vs. NN

# slides	a	b	c	d
1	0.05	0.6	4.5	0.6
>1	0.2	-1.8	14.9	5.5

Maximum tumour diameter vs. LS

# slides	a	b	c	d
1	0.08	-0.14	3.3	-1.3
>1	0.14	-0.5	3.1	20.7

Estimated square area vs. NN

# slides	a	b	c
1	-0.004	3.2	2.3
>1	0.002	4.2	-3.8

Estimated square area vs. LS

# slides	a	b	c
1	0.01	1.4	0.6
>1	0.002	3.4	-9.7
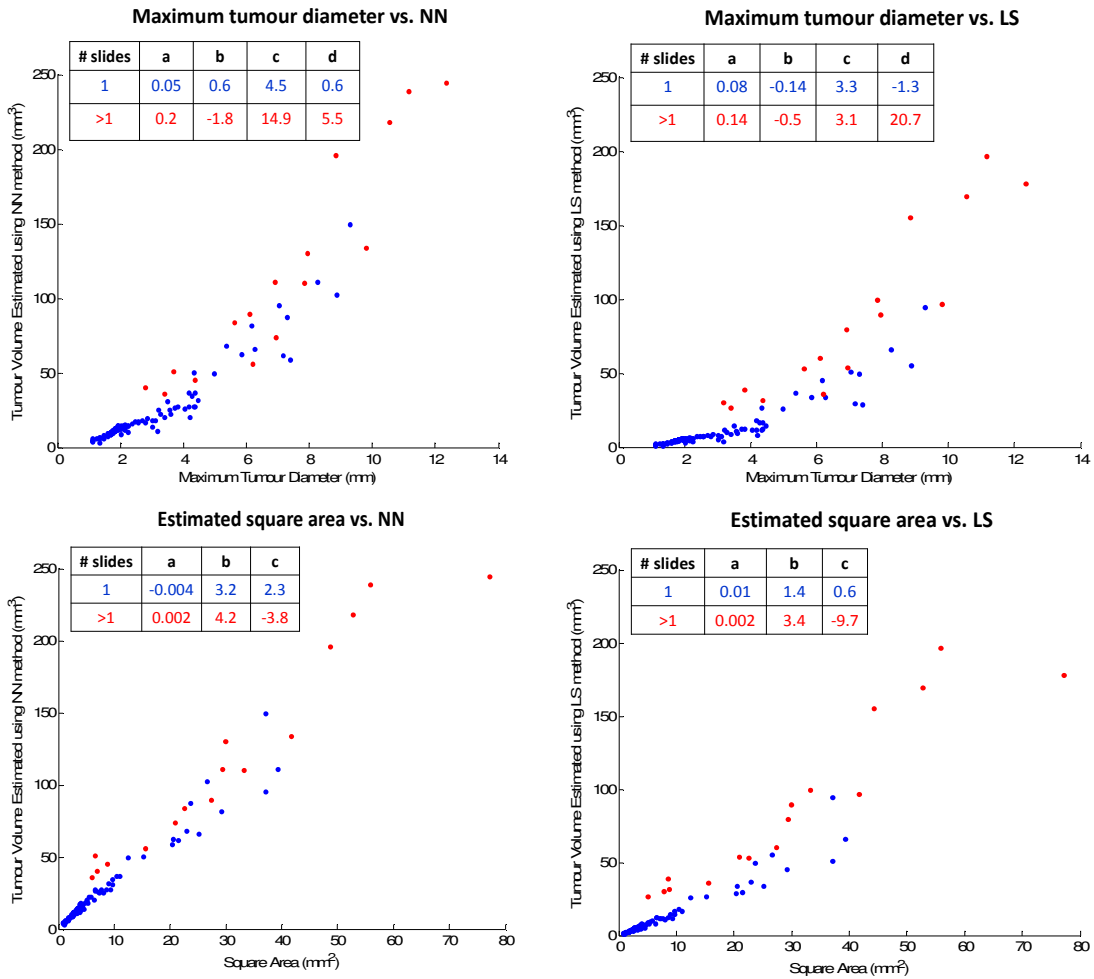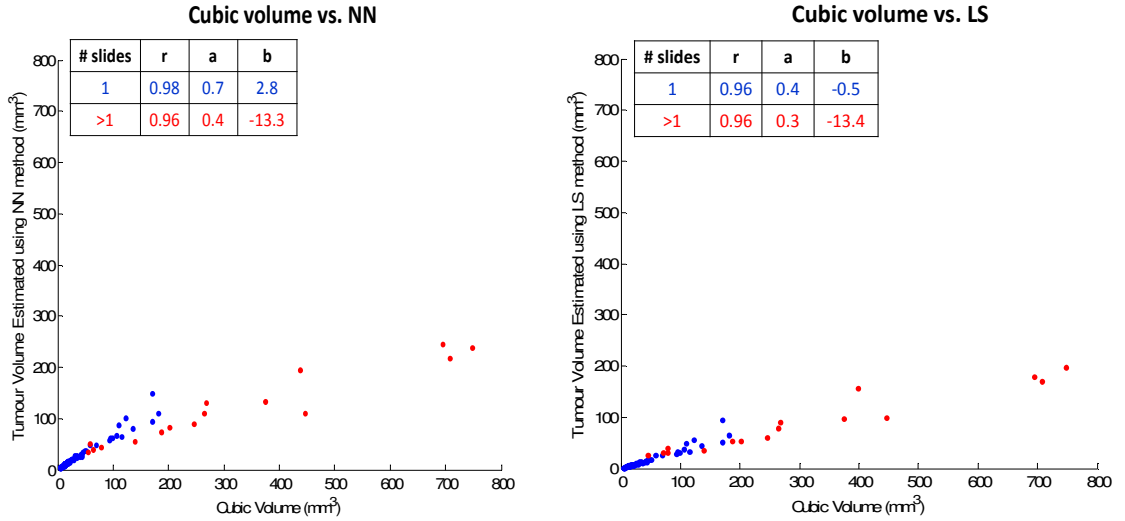
Figure 2.10. Scatter plots showing the relationship between the MTD (first row), ESA (second row), and CV (third row) tumour size estimation methods and the tumour volumes obtained from the NN approach (first column) and the LS approach (second column), under idealized tumour slicing assumptions. Blue points represent 1-slide tumours, and red points represent >1-slide tumours. For clarity of interpretation, two high-volume outliers (high-grade tumours with level set volumes of 480 mm^3 and 824 mm^3) were omitted from all graphs.
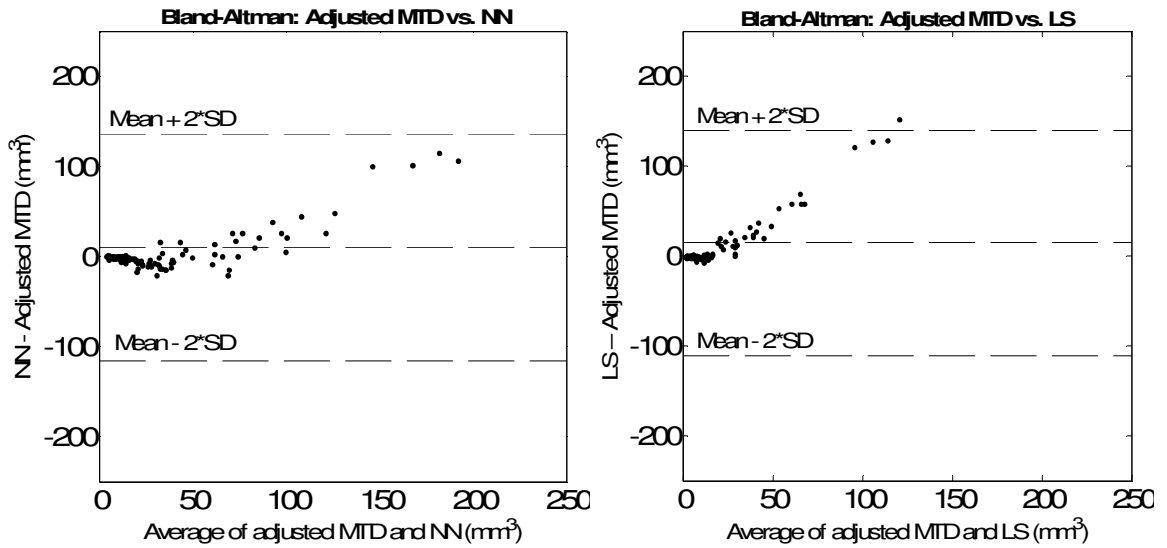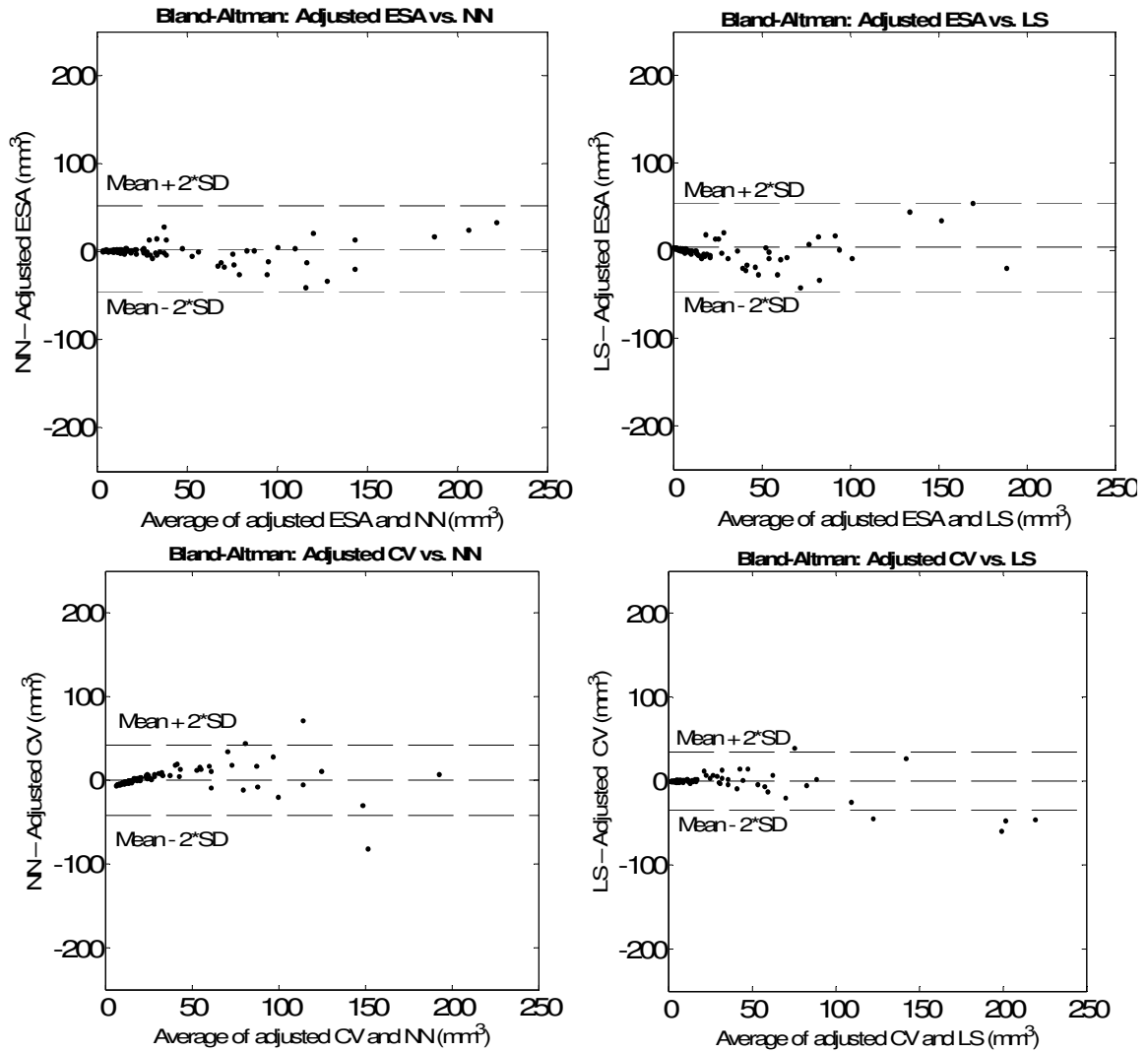
Figure 2.11. Bland-Altman plots of adjusted MTD (first row), ESA (second row), and CV (third row) tumour size estimation methods and the tumour volumes obtained from the NN approach (first column) and the LS approach (second column), under idealized tumour slicing assumptions. For clarity of interpretation, two high-volume outliers (high-grade tumours with level set volumes of 480 mm^3 and 824 mm^3) were omitted from all graphs.

Figure 2.12 shows histograms of the accuracy measurements of the NN and LS methods with respect to the MRI-determined tumour volumes on our fusion biopsy cohort, with the mean and standard deviation of the errors shown. Figure 2.13 shows Bland-Altman plots for the same data as shown in Figure 2.12. Analogous histograms to Figure 2.12 are shown in Figure 2.14 using the histology-determined 2D tumour areas

from our radical prostatectomy cohort, with corresponding Bland-Altman plots in Figure 2.15. Overall, these plots indicate that both the NN and LS methods are biased toward underestimating tumour size, as compared with reference standard tumour sizes on MRI and histology. However, the limits of agreement for the LS method are tighter, as compared to the limits of agreement for the NN method, as shown in Figures 2.13 and 2.15.
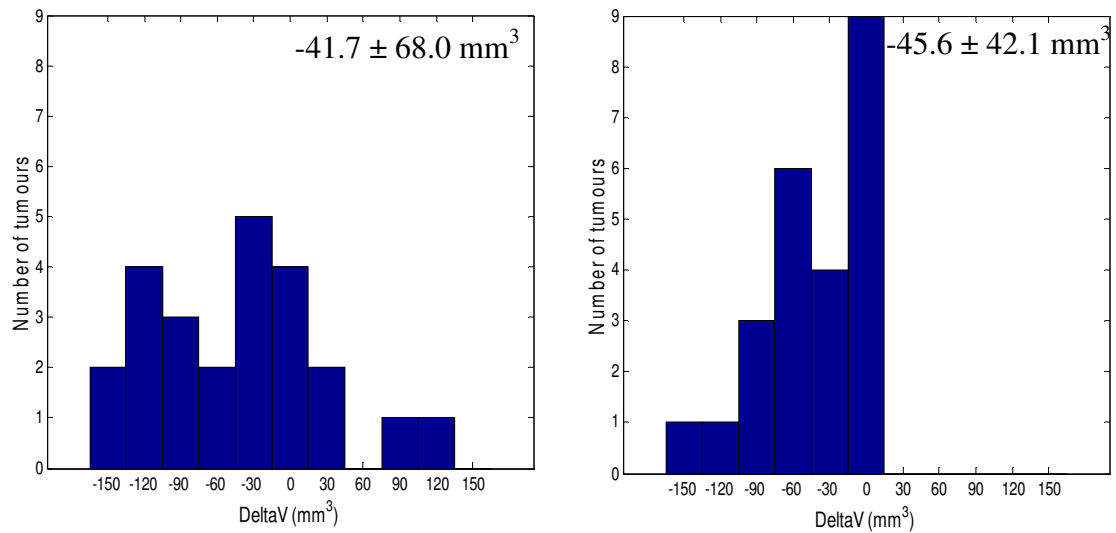
Figure 2.12. Histograms of differences in volume with respect to the 3D MRI-defined reference standard tumour volumes, with mean ± standard deviation overlaid. **Left:** DeltaV = NN-based volume – MRI reference volume. **Right:** DeltaV = LS-based volume – MRI reference volume.
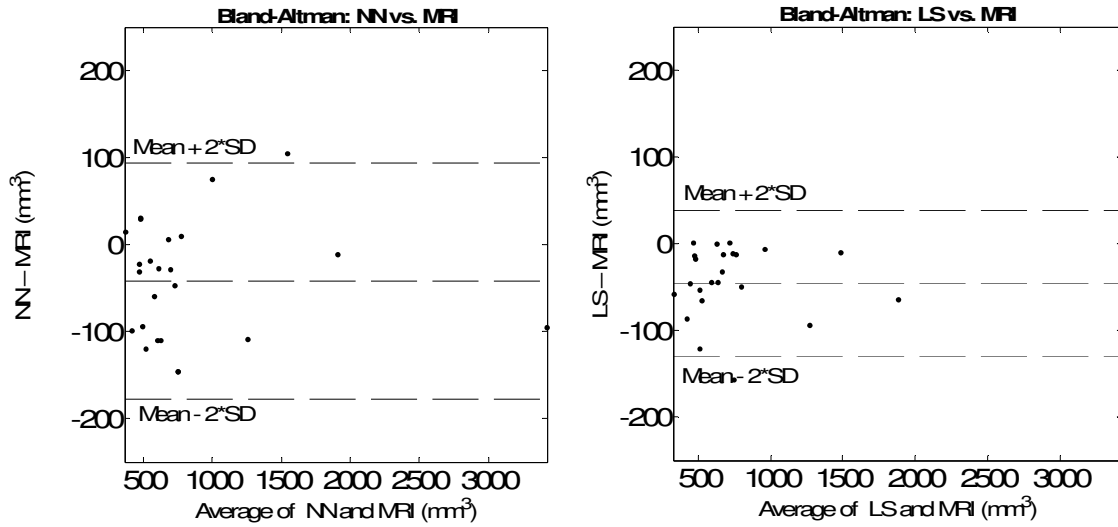
Figure 2.13. Bland-Altman plots of average and difference in NN-based volumes (**left**) volume and LS-based volumes (**right**) with respect to the 3D MRI-defined reference standard tumour volumes.
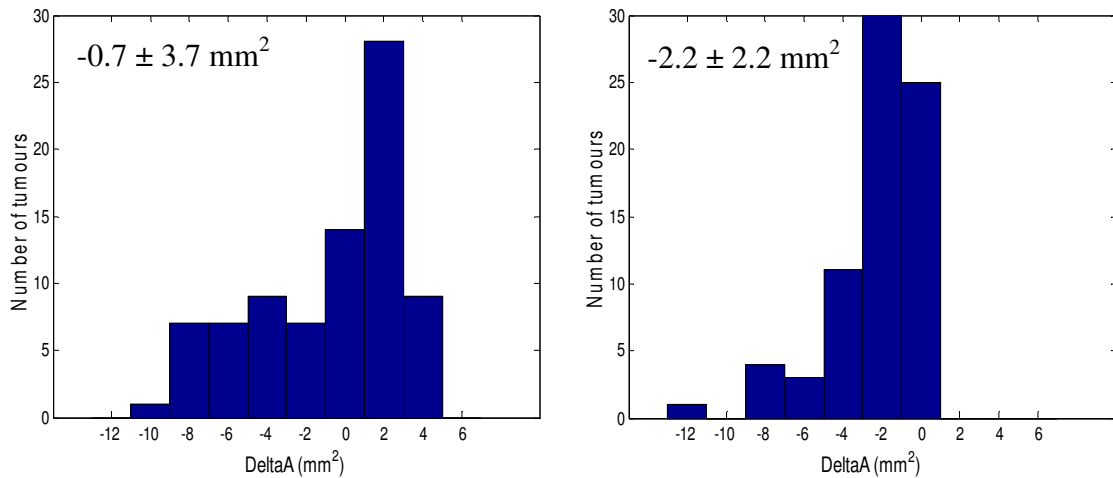
Figure 2.14. Histograms of differences in area with respect to the 2D histology-defined reference standard tumour areas, with mean ± standard deviation overlaid. **Left:** DeltaA = NN-based volume – reference volume. **Right:** DeltaA = LS-based volume – reference volume.
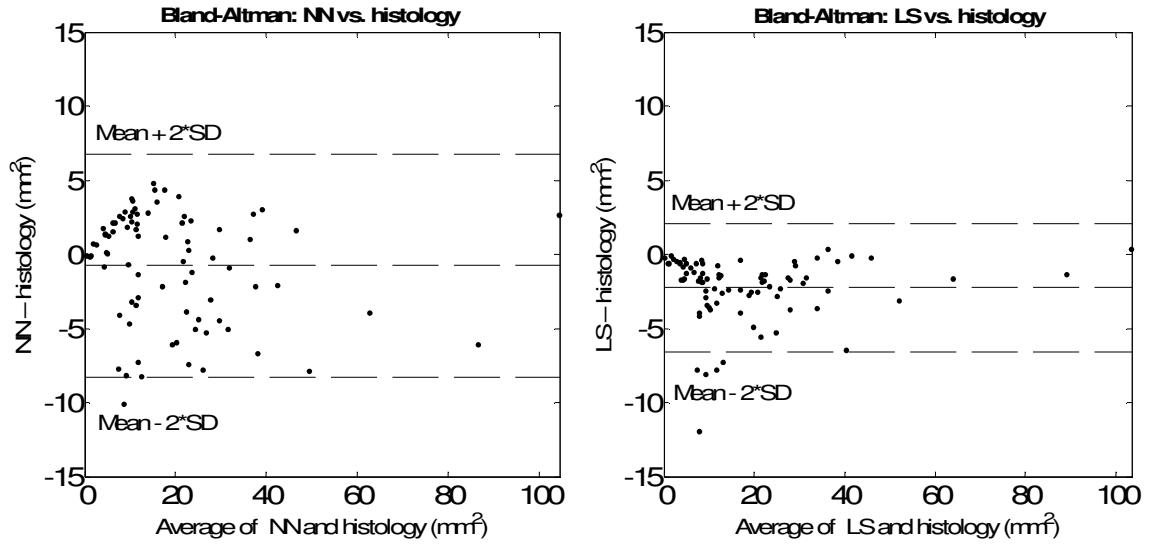
Figure 2.15. Bland-Altman plots of average and difference in NN-based areas (**left**) and LS-based areas (**right**) with respect to the 2D histology-defined reference standard tumour areas.

2.4.2 Assessment of impact of inter-slide spacing on variability of tumour volume estimation

We measured the variability of tumour volumes estimated using the NN and LS-based interpolation approaches as a function of inter-slide spacing. Figure 2.16 shows the standard deviations of the volumes reconstructed using NN and LS-based interpolation approaches versus inter-slide spacing values of 2, 3, 4, 5 and 6 mm. It is apparent on this figure that the variability of tumour volume estimates increases with increasing inter-slide spacing.
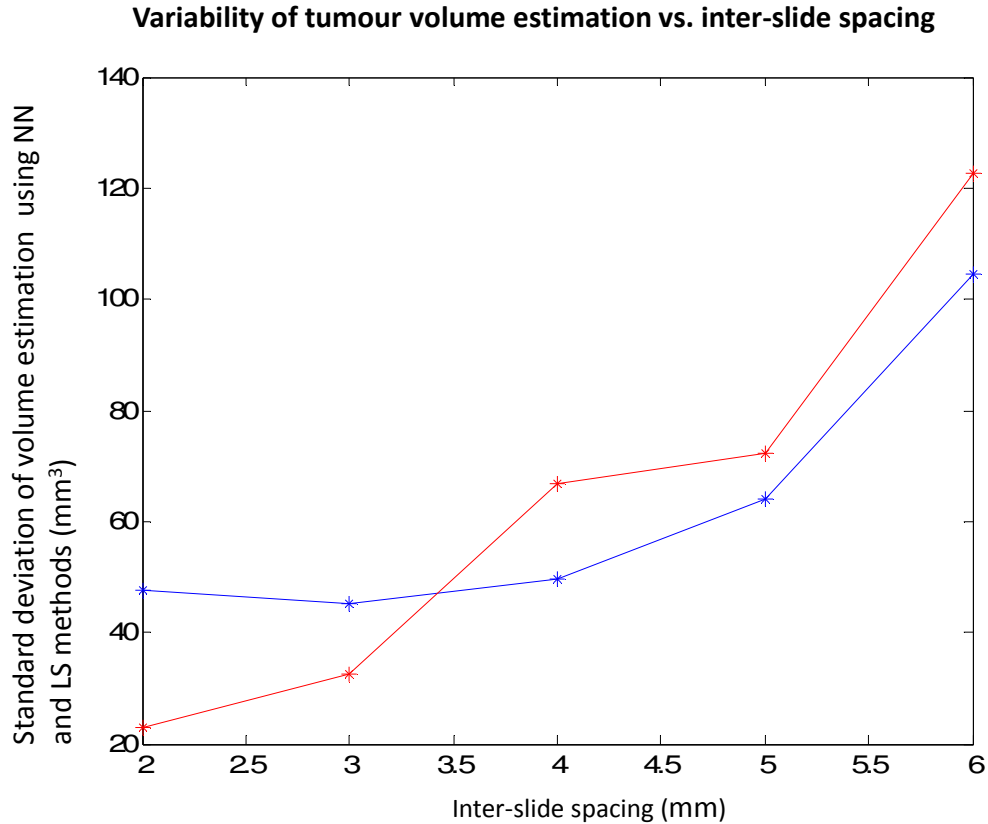
Figure 2.16. Tumour volume estimated via NN-based (blue) and LS-based (red) interpolation methods vs. inter-slide spacing of 2, 3, 4, 5 and 6.

2.5 Discussion

Several studies [25-29] have shown that the tumour volume measurement is an independent prognostic indicator that can predict the development of metastases, extraprostatic extension of the tumour, as well as overall survival in PCa patients. However, other studies have shown contradictory results [30-32]. These conflicting results could be attributed to the use of different tumour volume estimation approaches in the different studies, and use of methods which are subject to observer variability. Consequently, it has been suggested to utilize new technologies such as whole-slide digital histology imaging to support the repeatable measurement of tumour volume and address these issues [10].

An accurate and repeatable histologic tumour volume reference standard is valuable to studies validating imaging for appropriate treatment selection and guidance.

Radical prostatectomy, radiation therapy, cryotherapy, or high-intensity focused ultrasound (HIFU) can be used for whole-gland treatment of organ-confined prostate cancer. These treatments have frequent urinary, rectal, and sexual side effects. Although active surveillance may be an option for some patients, patients who fail active surveillance frequently subsequently receive conventional whole-gland treatment [33]. As a compromise between the extrema of radical therapy and active surveillance, focal therapy, or subtotal ablation, can be appropriate for patients with low-risk cancer characteristics, and is a technique that could allow the physician to eradicate all known foci of prostate cancer while minimizing damage to adjacent structures [34]. Focal therapy involves intensely treating the portion of the gland that contains significant tumour. This targeted treatment strategy has the potential to preserve the normal tissue and reduce the resultant side effects that are associated with removal or destruction of the entire prostate gland [35]. Focal therapy can be performed using several techniques, including thermo-ablative methods, using either heat or cold to destroy tumours, such as interstitial laser therapy, cryoablation and HIFU; radiation methods, such as brachytherapy; or chemical methods, such as regional alcohol injection [34]. Image–guided focal therapy depends on the validation of imaging modalities for detection and localization of cancer, and patient selection depends in part on tumour location and volume. Therefore, with the development of focal therapy, tumour burden assessment on imaging is becoming more valuable and a reliable histologic tumour volume reference standard is required for imaging validation studies [36].

In this work, we have developed a LS-based through-slide interpolation technique for estimating prostate tumour volume on digital histopathology images which produces smoother, potentially more plausible tumour shapes compared to a typically used NN-based technique. Our quantitative results show that using the LS-based technique, on average, estimates a lower tumour volume compared to the NN-based approach for both low-grade and high-grade tumours. It has been observed that the volumes calculated via the NN interpolation approach, which requires less sophisticated software for calculation, can be linearly adjusted to match those calculated via the LS-based interpolation approach. This suggests that for studies where the volume is the only measure of interest of the tumour, the NN-based technique may be sufficient. However, for imaging

validation studies where the precise tumour boundary location is of interest, the smooth boundaries produced by the LS technique may be a more plausible reference standard.

We observed that for the simpler tumour size estimation approaches (MTD, ESA, and CV), stronger relationships were found between the ESA and CV measures and the NN and LS measures, compared to the linear relationships found between the MTD and NN and LS measures. The MTD, ESA, and CV measures are 1-, 2-, and 3-dimensional, respectively. Our results suggest that the 1-dimensional MTD measurement, although straightforward to implement in a clinical pathology workflow, suffers from a relatively poorer relationship to tumour volume, as compared to the 2- and 3-dimensional approaches. If one is to resort to one of these more straightforward approaches, it would be worthwhile to use the ESA method at minimum; fortunately, the ESA can be calculated straightforwardly with only one additional measurement taken on the same slide on which the MTD is measured, so the incremental time cost of using the ESA method over the MTD method is likely to be small.

We observed a small difference in accuracy of the LS and NN tumour volume estimation approaches, with the LS approach yielding a slightly greater underestimation with respect to the MRI and histology-based reference standards. The LS method demonstrated less variability in error, suggesting that it is possibly less sensitive to variability in tumour shape.

Our data in Figure 2.16 indicate that there is a compromise between the variability of tumour volume estimation and inter-slide spacing; larger inter-slide spacing increases the variability of tumour volume estimation. However, decreasing the inter-slide spacing leads to an increase in the number of the digital histopathology slides and increases the cost of processing. Furthermore, inter-slide spacing values of less than 3 mm have been observed to cause tissue to warp excessively, rendering paraffin embedding challenging; 3 mm may be a practical lower limit for inter-slide spacing in a clinical pathology context. Our data suggest a rapid increase in variability of tumour volume estimation as inter-slide spacing rises beyond 5 mm. Overall, these data reinforce the current clinical standard approach of taking a slide every 3–5 mm, and support a decision to use a slide

spacing at the low end of this range for studies where precision of tumour volume estimation is important.

The results of our work need to be considered in the context of its assumptions and limitations. Because of a lack of ground truth contours between slides, evaluation of an interpolation approach is challenging; we resorted to using an MRI-based 3D reference standard, and performing our analysis in a reduced 2D space in order to evaluate the approach's ability to interpolate sparsely sampled 2D histology contours. Also, our current approach assumes that after 3D reconstruction, all histology slides are parallel, which is generally not the case due to variability in tissue cutting. Our ongoing work is intended to address both of these challenges.

In conclusion, level set-based through-slide interpolation of prostate tumours on digital pathology produces smoother 3D tumour surfaces that may be more biologically plausible than those produced via a typically used simpler nearest-neighbour interpolation. For cases where only tumour volume is of interest, the volumes produced via the simpler approach can be linearly adjusted to the level set-produced volumes, and the accuracies of volume estimation of the two approaches were similar. The smoother surfaces yielded by level set interpolation may be valuable to pathology-based imaging validation studies where tumour boundary location is important. In clinical scenarios where tumour contouring is impractical, volumes can be estimated based on 1-, 2-, or 3-dimensional tumour size measurements, with the 2-dimensional estimated square area on the largest histologic tumour cross section yielding a good compromise between efficiency and direct relationship to tumour volume estimated using planimetric approaches. Variability in histologic tumour volume estimation was found to increase with larger inter-slide spacing; for studies requiring the greatest repeatability of measurements of tumour volume, an inter-slide spacing of 3 mm is recommended.

2.6   References

1.   Howlader, N., et al., eds. *SEER Cancer Statistics Review, 1975-2009 (Vintage 2009 Populations), based on November 2011 SEER data submission, posted to the SEER web site*. 2012, NCI: Bethesda, MD.

2.   Chodak, G.W., et al., *Results of conservative management of clinically localized prostate cancer.* New England journal of medicine, 1994. **330**(4): p. 242-248.

3.   Burkhardt, J.H., et al., *Comparing the costs of radiation therapy and radical prostatectomy for the initial treatment of early-stage prostate cancer.* J Clin Oncol, 2002. **20**(12): p. 2869-75.

4.   Ward, J.F. and J.W. Moul, *Rising prostate-specific antigen after primary prostate cancer therapy.* Nature clinical practice. Urology, 2005. **2**(4): p. 174-82.

5.   Agarwal, P.K., et al., *Treatment failure after primary and salvage therapy for prostate cancer: likelihood, patterns of care, and outcomes.* Cancer, 2008. **112**(2): p. 307-14.

6.   Messing, E.M., et al., *Immediate versus deferred androgen deprivation treatment in patients with node-positive prostate cancer after radical prostatectomy and pelvic lymphadenectomy.* The lancet oncology, 2006. **7**(6): p. 472-9.

7.   Patel, A.R. and A.J. Stephenson, *Radiation therapy for prostate cancer after prostatectomy: adjuvant or salvage?* Nature reviews. Urology, 2011. **8**(7): p. 385-92.

8.   Egevad, L., J.R. Srigley, and B. Delahunt, *International Society of Urological Pathology (ISUP) consensus conference on handling and staging of radical prostatectomy specimens: rationale and organization.* Modern pathology : an official journal of the United States and Canadian Academy of Pathology, Inc, 2011. **24**(1): p. 1-5.

9.   Epstein, J.I., *An update of the Gleason grading system.* J Urol, 2010. **183**(2): p. 433-40.

10.   van der Kwast, T.H., et al., *International Society of Urological Pathology (ISUP) Consensus Conference on Handling and Staging of Radical Prostatectomy Specimens. Working group 2: T2 substaging and prostate cancer volume.* Modern

pathology : an official journal of the United States and Canadian Academy of Pathology, Inc, 2011. **24**(1): p. 16-25.

11.   Magi-Galluzzi, C., et al., *International Society of Urological Pathology (ISUP) Consensus Conference on Handling and Staging of Radical Prostatectomy Specimens. Working group 3: extraprostatic extension, lymphovascular invasion and locally advanced disease.* Modern pathology : an official journal of the United States and Canadian Academy of Pathology, Inc, 2011. **24**(1): p. 26-38.

12.   Monaco, J.P., et al., *High-throughput detection of prostate cancer in histological sections using probabilistic pairwise Markov models.* MIA, 2010. **14**(4): p. 617-629.

13.   Tabesh, A., et al., *Multifeature prostate cancer diagnosis and Gleason grading of histological images.* IEEE TMI, 2007. **26**(10): p. 1366-78.

14.   Gorelick, L., et al., *Prostate Histopathology: Learning Tissue Component Histograms for Cancer Detection and Classification.* IEEE Transactions on Medical Imaging (submitted), 2012.

15.   Montironi, R., et al., *Handling and pathology reporting of radical prostatectomy specimens.* Eur Urol, 2003. **44**(6): p. 626-36.

16.   Noguchi, M., et al., *Assessment of morphometric measurements of prostate carcinoma volume.* Cancer, 2000. **89**(5): p. 1056-64.

17.   Masanori Noguchi, et al., *Assessment of Morphometric Measurement of Prostate Carcinoma Volume.* American Cancer Society, September 2000. **89**(5): p. 1056–1064.

18.   Haffner, J., et al., *Peripheral zone prostate cancers: location and intraprostatic patterns of spread at histopathology.* The Prostate, 2009. **69**(3): p. 276-82.

19.   Chen, M.E., et al., *A streamlined three-dimensional volume estimation method accurately classifies prostate tumors by volume.* Am J Surg Pathol, 2003. **27**(10): p. 1291-301.

20.   Salarian, M., et al. *Toward Quantitative Digital Histopathology for Prostate Cancer: Comparison of Inter-Slide Interpolation Methods for Tumour Measurement*. in *SPIE Medical Imaging*. 2013. Orlando, Florida.

21.   Gibson, E., et al., *Registration of prostate histology images to ex vivo MR images via strand-shaped fiducials.* Journal of Magnetic Resonance Imaging, 2012.

22.   Osher, S. and J.A. Sethian, *Fronts propagating with curvature-dependent speed: Algorithms based on Hamilton-Jacobi formulations.* J Comp Phys, 1988. **79**: p. 12-49.

23.   Humphrey, P.A., *Complete histologic serial sectioning of a prostate gland with adenocarcinoma.* Am J Surg Pathol, 1993. **17**(5): p. 468-72.

24.   Andriy Fedorova, et al., *3D Slicer as an image computing platform for the Quantitative Imaging Network.* Magnetic Resonance Imaging, 2012. **30**(9): p. 1323-1341.

25.   Humphrey, P.A. and R.T. Vollmer, *Intraglandular tumor extent and prognosis in prostatic carcinoma: application of a grid method to prostatectomy specimens.* Hum Pathol, 1990. **21**(8): p. 799-804.

26.   McNeal, J.E., et al., *Patterns of progression in prostate cancer.* Lancet, 1986. **1**(8472): p. 60-3.

27.   Epstein, J.I., J.E. Oesterling, and P.C. Walsh, *Tumor volume versus percentage of specimen involved by tumor correlated with progression in stage A prostatic cancer.* J Urol, 1988. **139**(5): p. 980-4.

28. McNeal, J.E., et al., *Stage A versus stage B adenocarcinoma of the prostate: morphological comparison and biological significance.* J Urol, 1988. **139**(1): p. 61-5.

29. Vollmer, R.T., *Percentage of tumor in prostatectomy specimens: a study of American Veterans.* Am J Clin Pathol, 2009. **131**(1): p. 86-91.

30. Porten, S.P., M.R. Cooperberg, and P.R. Carroll, *The independent value of tumour volume in a contemporary cohort of men treated with radical prostatectomy for clinically localized disease.* BJU Int, 2010. **105**(4): p. 472-5.

31. Tineke Woltersa, et al., *Should pathologists routinely report prostate tumour volume? The prognostic value of tumour volume in prostate cancer.* European Urology, May 2010. **57**(5): p. 821–829.

32. Kikuchi E., S.P.T., Wheeler T.M., Slawin K.M., Ohori M., *Is tumour volume an independent prognostic factor in clinically localized prostate cancer?* J Urol, 2004. **172**: p. 508-511.

33. Koppie, T.M., et al., *Patterns of treatment of patients with prostate cancer initially managed with surveillance: results from The CaPSURE database. Cancer of the Prostate Strategic Urological Research Endeavor.* J Urol, 2000. **164**(1): p. 81-8.

34. Mouraviev, V., J.M. Mayes, and T.J. Polascik, *Pathologic basis of focal therapy for early-stage prostate cancer.* Nat Rev Urol, 2009. **6**(4): p. 205-15.

35. Jain, A.K. and R.D. Ennis, *Focal therapy, differential therapy, and radiation treatment for prostate cancer.* Adv Urol, 2012. **2012**(573193): p.1-6.

36. Marien, A., et al., *Target ablation-Image-guided therapy in prostate cancer.* Urol Oncol, 2014.

Chapter 3

3 Accuracy and variability of tumour burden measurement on multi-parametric MRI

3.1 Introduction

Early detection and accurate preoperative assessment of prostate cancer are crucial to the selection of appropriate treatment [1]. The combination of digital rectal examination (DRE), prostate-specific antigen (PSA) testing, and 2D transrectal ultrasound (TRUS)-guided biopsy has resulted in enhanced screening and diagnosis of prostate cancer, detecting smaller tumours at an earlier stage [2]. However, due in part to the high sensitivity and low specificity of screening, prostate cancer is currently over-diagnosed [3], potentially leading to unnecessary patient anxiety, diagnostic interventions, and aggressive whole-gland treatment (radiotherapy or prostatectomy surgery) with associated side effects. Approximately 40% of men with organ-confined PCa undergo radical prostatectomy, with nearly 80,000 surgeries each year in the United States [4]. Consequently, there is an increasing interest in the use of focal therapy for intermediate-risk cancers to treat localized prostate cancer while minimizing damage to the healthy tissue and surrounding organs [2]. *A non-invasive means for accurate determination of patient eligibility for focal prostate cancer therapy could be of substantial clinical value and an important step toward reduction of over-diagnosis and treatment.*

The determination of whether a patient is a candidate for focal therapy depends in part on prognosis, which is multi-factorial and known to be related to the tumour burden (i.e. the total volume of cancer), as well as Gleason grades of the tumours [5]. In addition, knowledge of the volumes and spatial distribution of tumours enables an assessment of the feasibility of focal therapy delivery effectively and safely. Biopsy yields approximately one dozen cylindrical 1 mm × 18 mm tissue samples and therefore

provides a tenuous estimate of tumour burden only under a strong set of assumptions. Emerging evidence suggests that multiparametric magnetic resonance imaging (MPMRI), with its morphological and functional pulse sequence capabilities, may permit accurate assessment of prostate cancer burden [6, 7], with implications for screening and targeting treatment. Typical pulse sequences used for prostate cancer imaging include T2-weighted (T2W), diffusion-weighted (DW) and dynamic contrast enhanced (DCE) images [8]. The accuracy of 1.5T MRI for prostate tumour volume determination has previously been measured for T2W and MR spectroscopic imaging [9] and for T2W, DCE, and DW imaging [10]. In both studies, the accuracy of MRI-measured tumour volumes was evaluated against a histopathologic reference standard, with spatial correspondence between MRI and histology established by qualitative image inspection or by a grid method. *The accuracy and inter-observer variability of prostate tumour volume estimation based on separate expert contouring of each of the T2W, DCE, and DW MRI sequences acquired using an endorectal coil at 3T is currently unknown.*

The objective of our study was to measure the accuracy, inter-observer variability, and inter-sequence variability of prostate tumour volume estimation based on contouring of T2E, DCE, and DW MRI acquired at 3T using an endorectal receive coil. Our reference standard for accuracy is based on a high-accuracy 3D histology reconstruction and registration to *in vivo* MRI [11], corresponding the MRI with adjusted NN-based reference standard histology tumour volumes. The method for 3D histology reconstruction and registration to *in vivo* MRI was developed by another member of our laboratory and is out of the scope of this thesis.

3.2 Materials

3.2.1 Materials and imaging

This study was approved by the human subject research ethics board of our institution, and written informed consent was obtained from all patients. The source population includes 10 patients who underwent radical prostatectomy between April 2010 and December 2011, selected from patients with biopsy-proven prostate cancer by three collaborating urologists/surgical oncologists. The inclusion criteria were: (1) age 18 years

or older, (2) clinical stage T1 or T2 prostate cancer histologically confirmed by biopsy, and (3) suitable for and consenting to radical prostatectomy. The exclusion criteria were: (1) prior therapy for prostate cancer, (2) use of 5-alpha reductase inhibitors within 6 months of the study start, (3) inability to comply with preoperative imaging, (4) allergy to contrast agents, (5) sickle cell or other anemias, (6) hip prosthesis, (7) sources of artifact within the pelvis, and (8) contraindications to MRI.

All MR images were acquired using a 3T GE Discovery MR750 (GE Healthcare, Waukesha, WI, USA). For T2W MRI, a 2D fast spin-echo sequence was used (repetition time: 4000–13000 msec, echo time: 156–164 msec, bandwidth: ±31.25 kHz, two signals acquired, field of view: 14 cm, slice thickness: 2.2 mm, slide spacing: 2.2 mm, matrix: 320×192, 40 slices, flip angle: 90º). For dynamic contrast enhanced MRI, a 3D spoiled gradient-recalled echo sequence was used (repetition time: 5.6–5.9 msec, echo time: 2.1–2.2 msec, bandwidth: ±31.25 kHz, one or two signals acquired, field of view: 14 cm, slice thickness: 2.8 mm, slice spacing: 1.4 mm, matrix: 256×192, 42 slices, flip angle: 15°; seven volumes acquired at 90 sec per volume). In addition, we acquired apparent diffusion (ADC) coefficient MR images. To generate ADC images, DW images were post-processed on the MR750 console. For DW images, a 2D echo-planar sequence was used (repetition time: 4000 msec, echo time: 70–77 msec, bandwidth: ±125 kHz, three signals acquired, field of view: 14 cm, slice thickness: 3.3–3.6 mm, slide spacing: 3.3–3.6 mm, matrix: 128×256, 20–34 slices, flip angle: 90º). Sample MR images are shown in Figure 3.1.

After radical prostatectomy, the prostate was fixed in 10% buffered formalin for 48 hours. Each specimen was then transversely sliced into 4.4 mm thick sections. The sections were paraffin embedded, yielding whole-mount H&E-stained microscope slides, each containing a single 4 µm-thick section of tissue taken from each block face. The histology slides were digitized using a ScanScope GL (Aperio Technologies, Vista, CA, USA) bright field slide scanner.
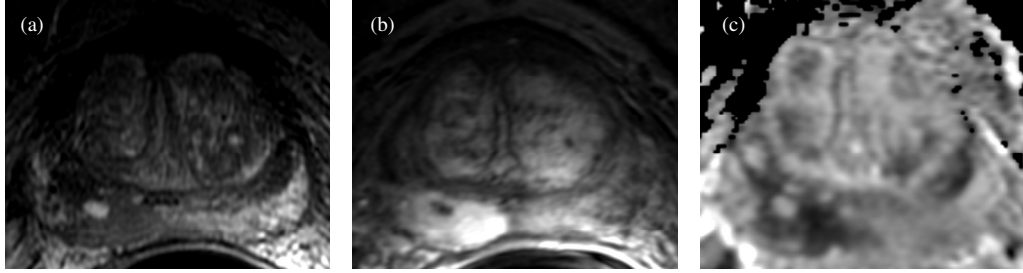
Figure 3.1. Samples of **(a)** T2W, **(b)** DCE, **(c)** ADC MPMRI for one patient; note the lesion in the bottom left of each image.

3.3 Tumour contouring

Three observers (a radiology resident, a radiology fellow, and a radiologist, all involved in prostate MRI reporting and research) assessed the MPMRI using the PI-RADS system [12] and delineated observed lesions separately on the T2W, DCE, and ADC images. All observers were blinded to the histology during the contouring. An experienced clinician, blinded to the MRI, contoured and graded all lesions on histology each image using the ScanScope ImageScope v11.0.2.725 software (Aperio Technologies, Vista, CA, USA) using a Cintiq 12WX pen-enabled display (Wacom Co. Ltd., Saitama, Japan); these contours were reviewed and edited as necessary by a genitourinary pathologist. Figure 3.2 shows contouring for one patient.
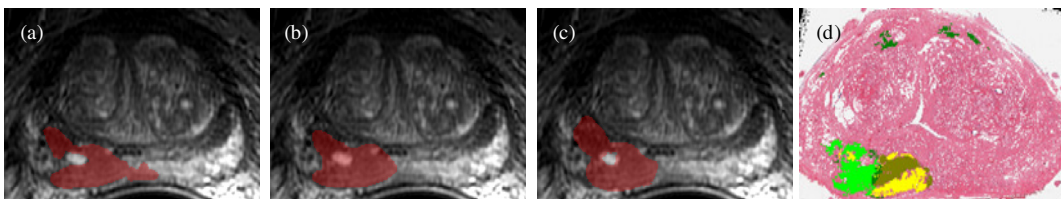
Figure 3.2. (a-c) Lesion contours from three different observers on the same T2W image. **(d)** Corresponding post-prostatectomy histology with lesion contoured. Light green: Gleason 3+4. Dark green: Gleason 3+3. Brown: Gleason 4+3. Yellow: Gleason 4+4.

3.4 Methods

3.4.1 Tumour volume calculation

On MPMRI, tumour volume was calculated as the number of voxels within each 3D contoured region, multiplied by the voxel size in mm^3. On histology, volume was measured by first multiplying the cross sectional area of each contoured region on each slide by the inter-slide spacing of 4.4 mm [hereinafter referred to as a *nearest neighbour* (NN) interpolation approach]. Due to the large inter-slide spacing, this approach implies implausible tumour surfaces having sharp transitions (Figure 3.3(a)). We have previously demonstrated [13] that a *level set* (LS)-based through-slide interpolation can produce smoother tumour surfaces (Figure 3.3(b)); these volumes may be more reasonably comparable to those defined on MRI (Figure 3.3(c)). We showed that the tumour volumes given by the LS approach can be estimated based on those given by the simpler NN approach using a linear regression ($LSVolume = m(NNVolume) + b$) where $m = 0.58, b = -2.2$ for tumours occupying only one slide, and $m = 0.82, b = -7.5$ for tumours occupying multiple slides [13]. In this work, we adjusted the calculated NN volumes according to these formulae, and then multiplied by a tissue shrinkage factor of 1.2 to compensate for shrinkage due to formalin fixation and tissue processing.
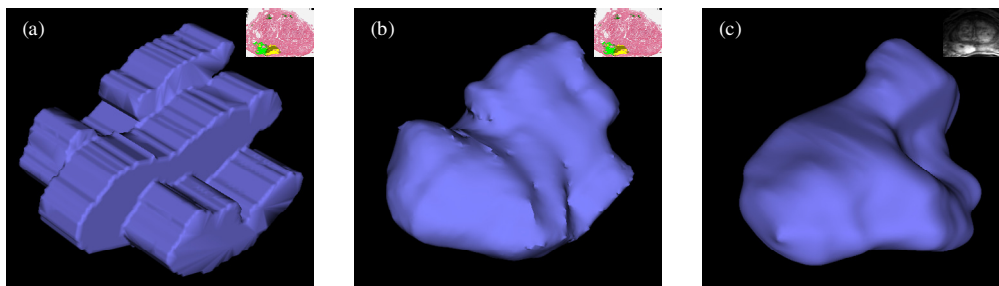
Figure 3.3. Tumour volume enclosed by **(a)** nearest-neighbour and **(b)** level set-based interpolation of histology contours. **(c)** Corresponding tumour surface from MRI contours.

3.4.2 Imaging-histology correspondence

Digitized histology images were reconstructed to the context of an ex vivo MRI acquired prior to sectioning using a submillimetre-accurate 2D-3D affine registration algorithm [11], and subsequently deformably co-registered to in vivo MPMRI via an interactive thin-plate spline approach with an overall error of 2 mm, measured as the post-registration misalignment of manually identified homologous intrinsic fiducial landmarks. The above steps were performed by another member of our laboratory and their details are out of the scope of this thesis.

Interactive exploration of the fused imaging and histology volumes was performed to establish correspondence between each contoured tumour on MPMRI and its corresponding contoured tumour on histology; only contoured MPMRI regions having corresponding histology tumours (i.e. true positives on MPMRI) were used in this study.

3.4.3 Statistical analysis

Due to small sample size, this is a hypothesis-generating study and therefore descriptive statistics were reported. We quantified error for each tumour as the MPMRI tumour volume measurement minus the histology tumour volume measurement; positive error values represent an overestimation of volume on MRI. To measure inter-observer and inter-sequence variability of tumour volume estimation on MPMRI, we selected the six tumours that were contoured by all three observers on all three sequences, where at least one MPMRI contouring of each tumour corresponded spatially to a histology-defined tumour. For each such tumour, we measured the standard deviation of the MPMRI volumes estimated by the three observers, and reported the inter-observer variability as the average of these standard deviations for the T2W, DCE, and ADC sequences separately. For each tumour, we measured the standard deviation of the MPMRI volumes given by each observer's contouring of that tumour on T2W, DCE, and ADC sequences, and reported the average of these standard deviations as the inter-sequence variability.

3.5 Results

The aggregate measurements of MPMRI tumour volume accuracy are provided in Table 3.1, with detailed results for each tumour in Figure 3.4. Overall, the MPMRI tumour volumes were overestimates of the histology tumour volumes, with the ADC maps providing the closest estimates and the DCE volumes providing the best correlation with histology volumes. For the MPMRI observer variability experiment, the tumour volume estimates are shown in Figure 3.5. The overall measured inter-observer variabilities were 245 mm^3, 196 mm^3, and 238 mm^3 for the T2W, DCE, and ADC sequences, respectively. The measured inter-sequence variabilities were 277 mm^3, 329 mm^3, and 320 mm^3 for observers 1, 2, and 3, respectively. The overall inter-sequence variability given by pooling all of the observers was 309 mm^3; detailed results are given in Figure 3.6. With the exception of one tumour, the average volume estimates on DCE were lower than those for T2W and ADC. The agreement between observers on each pulse sequence was superior to the inter-pulse sequence agreement even within individual observers.

Table 3.1. Differences between MPMRI and histology tumour volume estimates.

	# Tumours	D = MRI vol. - hist. vol. (mean ± std.)	D > 0	MRI vol. / hist. vol. (median)	Pearson's corr. (MRI vol.– hist. vol.)
T2W	27	907 ± 1804 mm^3	93% (25/27)	2.9	0.64 (p < 0.001)
DCE	24	1138 ± 2118 mm^3	88% (21/24)	2.8	0.93 (p < 0.001)
ADC	27	871 ± 1537 mm^3	85% (23/27)	2.6	0.81 (p < 0.001)
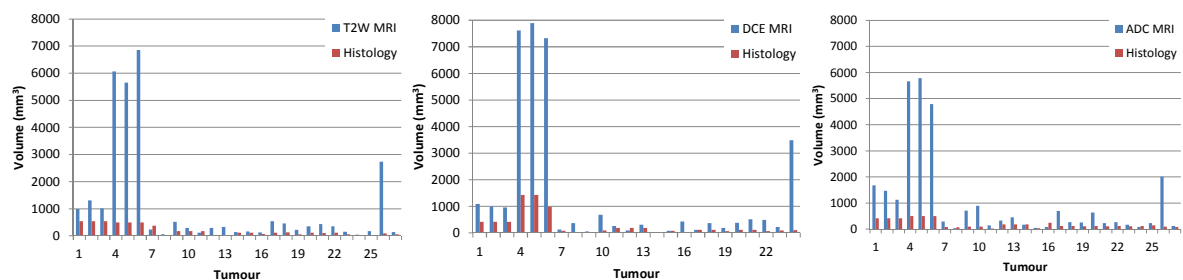
Figure 3.4. MPMRI and histology tumour volume estimates for **(a)** T2W, **(b)** DCE, **(c)** ADC.
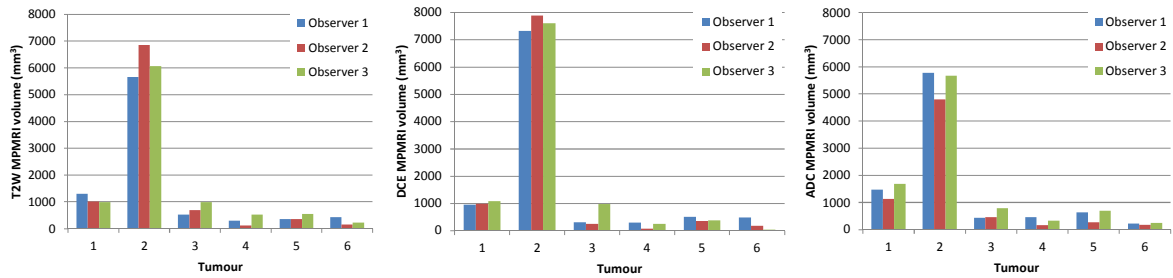
Figure 3.5. MPMRI volumes of six tumours delineated by three observers on **(a)** T2W, **(b)** DCE, and **(c)** ADC.
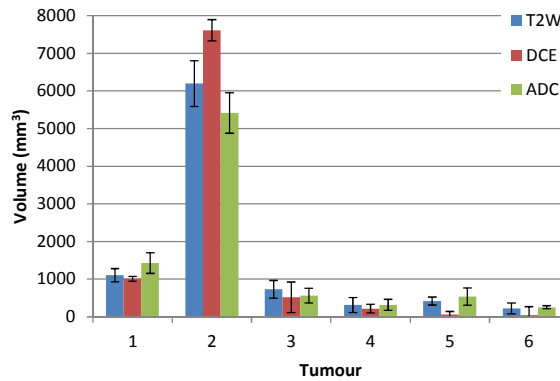
Figure 3.6. Mean±std tumour volume across all observers for each sequence.

3.6 Discussion

This is the first study measuring accuracy and variability in prostate tumour volume estimation on MPMRI at 3 Tesla, using separate contouring on T2W, DCE, and ADC. Tumour volume error estimation was supported by a highly accurate MPMRI-histology image registration and a smooth interpolation of planimetric tumour measurements on histology.

Prostate tumour volumes estimated based on multi-parametric MRI (T2W, DCE, ADC) consistently overestimated reference tumour volumes defined by a smooth interpolation of planimetric tumour contours on digitized histology images. Variability of tumour volume estimates across the different pulse sequences exceeded inter-observer variability within any sequence. Tumour volume estimates on DCE MRI provided the lowest inter-observer variability and the highest correlation with histology tumour volumes, whereas ADC provided the lowest volume estimation error. If validated on a

larger data set, the observed correlations could support the development of a correction scheme for estimation of tumour burden based on MPMRI volume estimates. These results may also be valuable to informing the design and validation of algorithms for automated segmentation of prostate tumours on MPMRI.

3.7 References

1. Nakashima, J., A. Tanimoto, Y. Imai, M. Mukai, Y. Horiguchi, K. Nakagawa, M. Oya, T. Ohigashi, K. Marumo, and M. Murai, *"Endorectal MRI for prediction of tumour site, tumour size, and local extension of prostate cancer,"* Urology, 2004. **64**(1): p. 101-5.

2. *Turkbey, B., P.A. Pinto, and P.L. Choyke, "Imaging techniques for prostate cancer: implications for focal therapy," Urology, 2012. 188(4): p. 191-203.*

3. Welch, H.G. and W. C. Black, *"Overdiagnosis in Cancer,"* Journal of the National Cancer Institute, *2010.* **102**(9): p. 605-613.

4. Burkhardt, J.H., M.S. Litwin, C.M. Rose, R.J. Correa, J.H. Sunshine, C. Hogan, and J.A. Hayman, *Comparing the costs of radiation therapy and radical prostatectomy for the initial treatment of early-stage prostate cancer.* J Clin Oncol, 2002. **20**(12): p. 2869-75.

5. Egevad, L., J.R. Srigley, and B. Delahunt, *International Society of Urological Pathology (ISUP) consensus conference on handling and staging of radical prostatectomy specimens: rationale and organization.* Modern pathology : an official journal of the United States and Canadian Academy of Pathology, Inc, 2011. **24**(1): p. 1-5.

6. Villeirs, G.M., W. Oosterlinck, E. Vanherreweghe, and G.O. De Meerleer, *"A qualitative approach to combined magnetic resonance imaging and spectroscopy in the diagnosis of prostate cancer,"* European Journal of Radiology, 2007. **73**(2): p. 352-356.

7. Ahmed, H.U., A. Kirkham, M. Arya, R. Illing, C. Allen, and M. Emberton, *"Is it time to consider a role for MRI before prostate biopsy,"* Nature Reviews Clinical Oncology, 2009, **6**(4): p. 197-206

8. Engelbrecht, M.R., J.O. Barentsz, G.J. Jager, M. Van Der Graaf, A. Heerschap, J.P.M. Sedelaar, R.G. Aarnink, and J.J.M.C.H De La Rosette, *" prostate cancer staging using imaging,"* BJU International 86, 2000. **86**(s1): p. 123-134.

9. Coakley, F.V., P.H. Choi, C.A. Gougoutas, B. Pothuri, E. Venkatraman, D. Chi, A. Bergman, and , H. Hricak, *"Pertoneal Metastases: Detection with Spiral CT in Patients with Ovarian Cancer,"* Radiology, 2002. **223**(2).

10. Isebaert, S., L. Van den Bergh, K. Haustermans, S. Joniau, E. Lerut, L. De Wever, F. De Keyzer, T. Budiharto, P. Slagmolen, H. Van Poppel, and R. Oyen, *"Multiparametric MRI for proatate cancer localization in correlation to whole-mount histopathology,"* Journal of Magnetic Resonance Imaging, 2013. 37(6): p. 1392-1401.

11. Gibson, E., C. Crukley, M. Gaed, J.A. Gomez, M. Moussa, J. Chin, G. Bauman, A. Fenster, and A.D. Ward, *"Registration of prostate histology images to ex vivo MR images via strand-shaped fiducials,"* Journal of Magnetic Resonance Imaging, 2012. **36**(6): p. 1402-1412.

12. Barentsz, J.O., J. Richenberg, R. Clements, P. Choyke, S. Verma, G. Villeirs, O. Rouviere, V. Logager, and J.J. Fütterer, *ESUR prostate MR guidelines 2012.* European Radiology, **22**(4), 2012: p. 746-757.

13. Salarian, M., M. Shahedi, E. Gibson, M. Gaed, J.A. Gomes, M. Moussa, G.S. Bauman, and A.D. Ward, *"Toward Quantitative Digital Histopathology for Prostate Cancer: Comparison of Inter-Slide Interpolation Methods for Tumour Measurement,"* SPIE Medical Imaging, 2013.

Chapter 4

4   Summary and discussion

This thesis summarized the importance of prostate tumour volume measurement and its use in the appropriate therapy selection for each individual patient. Assessment of accurate pathologic reporting including assessment of tumour volume in the post-prostatectomy specimen is important to determining the need of life-saving adjuvant therapy. In addition, prostate tumour volume measurement can be used to evaluate the suitability and feasibility of focal therapy, which can potentially spare patients the deleterious side effects of radical treatment.

Since reliable estimates of histologic tumour volume require a well-motivated method to inter-slide tumour boundary interpolation, we have implemented a 3D reconstruction algorithm that utilizes smooth interpolation and extrapolation to reconstruct prostate tumour volumes from prostate 2D digital histology images. Specifically, we have implemented a LS-based through-slide interpolation method to estimate prostate tumour volumes and compared its estimates to those given by the planimetric NN-based interpolation method. In addition, the relationships between the tumour volumes estimated using NN and LS-based interpolation methods, and the maximum tumour diameter (MTD), estimated square area (ESA), and cubic volume (CV) methods to tumour size estimation were investigated. We measured the accuracy of the LS-based interpolation method for tumour boundary interpolation in comparison to the NN method by reconstructing prostate tumour volumes with different shapes using 3D MRI tumours as a reference standard. Furthermore, we have measured the accuracy of tumour area estimation using NN and LS-based interpolation methods using 2D histology-defined tumours as another reference standard. We also assessed the sensitivity of histologic tumour volume estimation to inter-slide spacing. Specifically, we estimated the standard deviation of the tumour volume estimates using a practical range of different inter-slide spacing values.

These experiments produced the following main conclusions in Chapter 2:

1) The LS-based interpolation method on digital histology images produces smoother 3D tumour surfaces that may be more biologically plausible, as compared to those produced via the NN-based interpolation method.

2) The NN method on digital histology images produces larger tumour volumes, compared to the LS method, by a median factor of 2.3.

3) Where tumour volume is of interest, the volumes calculated via the NN-based interpolation method, which is more translatable to a clinical workflow, can be linearly adjusted to those calculated via the LS-based interpolation method on digital histology images. However, where tumour boundary localisation is important, the LS-based approach provides a more plausible boundary.

4) Where simpler tumour volume estimation methods based on linear measurements are to be used, it is advisable to use, at minimum, a two-dimensional measurement such as the ESA approach, as opposed to a one-dimensional measurement of tumour diameter.

5) There is a linear relationship between MRI reference tumour volumes and MRI tumour volumes estimated via the NN and LS-based interpolation methods. In addition, we observed tighter limits of agreement between the LS-based volume estimates and the MRI reference standard, as compared to the NN-based volume estimates.

6) There is a linear relationship between 2D histology-defined reference standard tumour areas and 2D histology tumour areas estimated via NN and LS-based interpolation methods. In addition, we observed tighter limits of agreement between the LS-based area estimates and the histologic reference standard, as compared to the NN-based area estimates.

7) Optimal inter-slide spacing involves a compromise between the consistency of volume estimation given by smaller spacing and the cost and practical challenges associated with histotechnical handling of thin whole-mount slices. The variability of histologic tumour volume estimation decreases with decreased inter-slide spacing, and this variability increases sharply for inter-slide spacing larger than 5 mm.

We used our level set based histologic tumour volume estimates to evaluate prostate tumour volumes estimated based on expert observers' contouring of MPMRI. Specifically, we measured the accuracy, inter-observer variability, and inter-sequence variability of radiologists' tumour volume estimates on T2W, DCE, and ADC images acquired at 3 T using an endorectal receive coil by comparison to a histologic reference standard.

These experiments produced the following main conclusions in Chapter 3:

1) Tumour volumes measured on MPMRI consistently overestimated the histological reference tumour volumes as measured via LS-based interpolation on digital histology images.

2) Tumour volumes estimated on DCE MRI provided the highest correlation with histology tumour volumes, whereas tumour volumes estimated on ADC maps provide the closest estimates of the histology tumour volumes.

3) The average tumour volume estimated on DCE images is lower than the tumour volumes estimated on T2W and ADC images.

4) Inter-sequence variability in tumour volume estimation exceeded inter-observer variability.

Chapter 5

5   Future work

Future work stemming from this thesis includes: (1) the reconstruction of 3D histology tumour volumes from non-parallel digitized 2D histology slides; (2) studying the effect of confounders such as atrophy, benign prostatic hyperplasia (BPH) and prostatic intra-epithelial neoplasia (PIN) on the appearance of lesions and their surrounding areas on MRI; and (3) studying the impact of inter-observer and inter-sequence variability in tumour contouring on histologic tumour coverage for focal therapy planning.

Some 3D histology reconstruction approaches assume that adjacent histology slides are parallel and evenly spaced only micrometers apart, and attempt to correct the deformations resulting from the histology acquisition procedure by aligning adjacent slides based on anatomical similarity or aligning each slide to a reference image taken during serial sectioning in a standard reference frame [1-3]. Other approaches include guiding specimen slicing to obtain histology slides with known positions and orientations [4], or using reference images taken throughout cutting, or from the sections before embedding or after the sectioning process [5]. However, these approaches are generally not compatible with clinical pathology processes. Due to several aspects of the clinical pathology process, prostate tissue histology sections are not generally parallel and equally spaced [6]. Histology slides are typically spaced every 3–5 mm and a single histology section is taken from each slide to save as much tissue as possible for later diagnosis if necessary. In addition, sections are typically cut in clinical facilities by hospital histotechnologists, with accompanying operator variability. These constraints break assumptions used by parallel slide reconstruction: adjacent slides are spaced millimeters apart and are generally not parallel [6], and the clinical pathology laboratory environment does not have the facilities for acquiring reference images (e.g. block face images) during sectioning. Thus, to support smooth tumour shape interpolation in the context of an

accurate 3D histology reconstruction [7], an interpolation approach that does not assume parallel slides would be valuable.

Differentiation of prostate cancer from benign confounders such as atrophy, BPH and prostatic intraepithelial neoplasia (PIN) is an important challenge to accurate MRI-based assessment of tumour burden [8, 9]. Atrophy occurs frequently in the prostates [10] of older men, and also is one of the most frequent histologic mimics of prostatic adenocarcinoma. With atrophy, some of the normal characteristics of the prostate glands are lost. BPH begins in the transition zone and grows inward toward the prostate core, tightening the urethra. Finally, PIN is essentially the finding of cells having a malignant appearance on the inside of the gland. Some PIN cells break through the basement membrane into the surrounding tissue and become invasive, whereas some PIN does not progress to cancer [10].

Separating these confounders from prostate cancer is challenging on MRI, and the current Prostate Imaging Reporting and Data Standard (PI-RADS) guidelines for prostate MRI interpretation do not provide guidelines regarding differentiating between specific confounders and prostate cancer [11]. In conjunction with a co-registered 3D histologic reference standard, imaging characteristics of these confounders on the different MRI sequences could be used to improve the PI-RADS standard and, subsequently increase reader performance in prostate tumour volume estimation and boundary delineation.

The accurate and repeatable delineation of dominant lesions on MPMRI is critical and challenging for enabling the clinical application of focal therapy, maximizing the treatment while minimizing damage to surrounding healthy tissue and nearby organs. It has been shown that tumour boundaries extended into the central zone may have been partially obscured by adjacent benign hyperplastic tissue. We observed substantial inter-observer and inter-sequence variability in tumour volume estimation on MPMRI. This variability injects uncertainty into clinical investigations of focal therapy, and may represent a barrier to the clinical implementation of focal therapy using MPMRI. It remains to be seen whether this variability has a clinically important impact on the

resulting histologic tumour coverage of focal therapy plans, and this would be an important question to study in the future.

5.1   References

1.   Andreasen, A., Drewes, A. M., Assentoft, J. E., and Larsen, N. E., *Computer-assisted alignment of standard serial sections without use of artificial landmarks. A practical approach to the utilization of incomplete information in 3-D reconstruction of the hippocampal region.* 1992. **45** (3): p. 199-207

2.   Verbeek, F., *Three-dimensional reconstruction of biological objects from serial sections including deformation correction.* Delft Technical University 1995.

3.   Alic, L., et al., *Facilitating tumor functional assessment by spatially relating 3D tumor histology and in vivo MRI: image registration approach.* PLoS One, 2011. **6**(8): p. e22835.

4.   Chen, L.H., Ho, H., Lazaro, R., Thng, C. H., Yuen, J., Ng, W. S., and Cheng, C., *Optimum slicing of radical prostatectomy specimens for correlation between histopathology and medical images.* Int J Comput Assist Radiol Surg 2010. **5**(5): p. 471-87.

5.   Jackson, A.S., et al., *Dynamic contrast-enhanced MRI for prostate cancer localization.* Br J Radiol, 2009. **82**(974): p. 148-56.

6.   Gibson, E., et al., *3D prostate histology image reconstruction: Quantifying the impact of tissue deformation and histology section location.* J Pathol Inform, 2013. **4**: p. 31.

7.   Gibson, E., et al., *Registration of prostate histology images to ex vivo MR images via strand-shaped fiducials.* Journal of Magnetic Resonance Imaging, 2012.

8.   Hoeks, C.M., et al., *Transition zone prostate cancer: detection and localization with 3-T multiparametric MR imaging.* Radiology, 2013. **266**(1): p. 207-17.

9.   Bratan, F., Niaf, E., Melodelima, C., Chesnais, A. L., Souchon, R., Mege-Lechevallier, F., Colombel, M., and Rouviere, O., *Inuence of imaging and histological factors on prostate cancer detection and localisation on multiparametric MRI: a prospective study.* Eur Radiology 2013: p. 1-11.

10.   G.J.S. Litjens, R.E., N. Shih, M. Feldman, J.O. Barentsz, C.A. Hulsbergen - van de Kaa, I. Kovacs, H.J. Huisman and A. Madabhushi, *Distinguishing prostate cancer from benign confounders via acascaded classifier on multi-parametric MRI.*, in *SPIE Medical Imaging 2014: Computer-Aided Diagnosis*2014.

11.   Barentsz, J.O., et al., *ESUR prostate MR guidelines 2012.* Eur Radiol, 2012. **22**(4): p. 746-57.

Appendix

Permission

Subject: Request for getting permission
From: Mehrnoush Salarian
To: reprint_permission
Date: Friday, April 11, 2014 1:00 PM

Dear Mehrnoush,

Thank you for seeking permission from SPIE to reprint material from our publications. As author, SPIE shares the copyright with you, so you retain the right to reproduce your paper in part or in whole.

Publisher's permission is hereby granted under the following conditions:

(1) the material to be used has appeared in our publication without credit or acknowledgment to another source; and

(2) you credit the original SPIE publication. Include the authors' names, title of paper, volume title, SPIE volume number, and year of publication in your credit statement.

Sincerely,
Karen Thomas for

Eric Pepper, Director of Publications
SPIE

Hello,

My name is Mehrnoush Salarian from The University of Western Ontario, Canada. I have submitted two papers of my work to SPIE Medical Imaging conference on 2013 and 2014. I presented these two papers in Orlando and San Diego, respectively.

Now, I am writing my thesis to finish my Master's. As I understood, I need a permission to use my two previous published papers. Could you please let me what should I do to get this permission. You can see my two papers' information as follows:

My SPIE 2013 paper's title: Toward quantitative digital histopathology for prostate cancer: comparison of inter-slide interpolation methods for tumour measurement

Proc. SPIE 8676, Medical Imaging 2013: Digital Pathology, 86760F (March 29, 2013); doi:10.1117/12.2007103

My SPIE 2014 paper's title: Accuracy and variability of tumour burden measurement on multi-parametric MRI

Thank you so much in advance.

Regards,
Mehrnoush

Curriculum vitae

Mehrnoush Salarian

The University of Western Ontario
London Regional Cancer Centre

EDUCATION:

May 2012 – Present

Master's Student, Biomedical Engineering, Imaging

The University Of Western Ontario, Biomedical Engineering Graduate Program, London, Ontario, Canada

Thesis Title: *"Prostate Tumour Volume Measurement on Digital Histopathology and MRI"*

Supervisor: Dr. Aaron D. Ward

Advisory committee members: Dr. Aaron Fenster and Dr. Glenn S. Bauman

GPA: 3.8 / 4

September 2009 – January 2012

M.Sc., Biomedical Engineering, Bioelectric Engineering

Amirkabir University of Technology, Faculty of Biomedical Engineering (Center of Excellence), Tehran, Iran

Thesis Title: *"A System for the Assessment and Processing of Infant Cry to Recognize Pathologies in Recently Born Babies"*

Supervisor: Dr. Mohammad Hasan Moradi

Co-Supervisor: Dr. Mansour Vali

September 2003 – July 2008

B.Sc., Electrical Engineering, Electronic Engineering

South Tehran Branch, Islamic Azad University (IAU), Tehran, Iran

Thesis Title: "*Real-Time ECG Transmission via Computer for Non-Clinical Applications*"

Supervisor: Dr. Ali Farokhi

GPA: 16.31 / 20

HONORS AND AWARDS:

• Western Graduate Research Scholarship (WGRS) and Western Graduate Research Scholarship International (WGRSI) (May 2012–April 2014)

• Ranked **150**th in the nationwide entrance exam of Iran among more than 30,000 participants, June 2009

• Ranked **2**nd among 300 Electrical Engineering, Electronic Engineering students, South Tehran Branch in Spring 2007 semester with **GPA** of **18.02/20**

• Top student among 300 Electrical Engineering, Electronic Engineering students, South Tehran Branch in Fall 2003 and Winter 2003 semesters with **GPA** of **17.20/20** and **18.08/20**, respectively.

RESEARCH EXPERIENCE:

• **Image-Guided Cochlear Implant Surgery**

  Image-Guided Intervention Course, Winter 2013

  Instructor: Dr. Terry Peters

• **3D Registration of The Time Series of the Prostate Dynamic Contrast-Enhanced Magnetic Resonance Images to Each Other**

  Advanced Image Processing and Analysis Course, Winter 2013

Instructor: Dr. Aaron D. Ward

- **An Iris Recognition Based on Dual Tree Complex Wavelet Transform**

  Advanced Digital Signal Processing Course, Spring 2010

  Instructor: Dr. Farshad Almasganj

- **High-Resolution Cry Analysis in Preterm Newborn Infants**

  Biomedical Signal Processing Course Project, Winter 2010

  Instructor: Dr. Mohammad Hasan Moradi

- **A Comparative Analysis of Fundamental Frequency Estimation Methods with Application to Pathological Voices**

  Biomedical Signal Processing Course Project, Winter 2010

  Instructor: Dr. Mohammad Hasan Moradi

- **Real-Time ECG Transmission via Computer for Non-clinical Applications**

  Bachelors Degree Thesis Project, Summer 2008

  Supervisor: Dr. Ali Farokhi

RELEVANT COURSES:
- Advanced Image Processing and Analysis
- Introduction to Digital Image Processing
- Principles of Communication and Knowledge
- Research Ethics and Biostatistics
- Biomedical Signal Processing
- Digital Signal Processing
- Advanced Digital Signal Processing
- Neural Network
- Physiology
- Anatomy
- Bioinstrumentation
- Electrophysiology

TEACHING EXPERIENCE:

- **Process Dynamic and Control:**

  The University Of Western Ontario, London, Ontario, Canada, Winter 2014

- **C++ Programming Fundamentals for Engineers:**

  The University Of Western Ontario, London, Ontario, Canada, Winter 2013

- **Electronic 1:**

  Sama Technical and Vocational Training School, Islamic Azad University, Noor   Branch, Noor, Iran, Fall 2010

- **Linear Control Systems:**

  Maziar University, Noor, Iran, Spring 2009

PUBLICATIONS:

Conference Presentations:

Oral Presentation:
- **Salarian M.,** Gibson E., Shahedi M., Gaed M., Gomez J. A., Moussa M., Romangnoli C., Cool D. W., Bastian-Jordan M., Chin J., Bauman G. S., and Ward A. D., "Accuracy and variability of tumour burden measurement on multi-parametric MRI", **SPIE Medical Imaging,** San Diego, California, USA (February 16-21, 2014).

- **Salarian M.,** Shahedi M., Gibson E., Gaed M., Gomez J. A., Moussa M., Bauman G. and Ward A., "Imaging Validation and Quantitative Pathology for Prostate Cancer Treatment Planning: Shape Interpolation Methods for Tumour Measurement", **CARO COMP Joint Scientific Meeting,** Montreal, Quebec, Canada (September 18-21, 2013).

- **Salarian M.,** Shahedi M., Gibson E., Gaed M., Gomez J. A., Moussa M., Bauman G. and Ward A., "Toward Quantitative Digital Histopathology for Prostate Cancer: Comparison of Inter-Slide Interpolation Methods for Tumour Measurement", **SPIE Medical Imaging**, Orlando, Florida, USA (February 9-14, 2013).

- **Salarian M.,** Vali M. and Moradi M. H., "Classification of Pain and Hunger Cries of Infants", **Iranian Conference on Electrical Engineering (ICEE)**, Tehran, Iran (May 15-17, 2012).

- Molaeezadeh S. F., **Salarian M.** and Moradi M. H., " Type-2 Fuzzy Pattern Matching for Classifying Hunger and Pain Cries of Healthy Full-term Infants", **The 16th CSI International Symposium on Artificial Intelligence and Signal Processing (AISP)**, Shiraz, Iran (May 2-3, 2012).

Poster Presentation:
- **Salarian M.**, Shahedi M., Gibson E., Gaed M., Gomez J. A., Moussa M., Bauman G. S., and Ward A. D., " Accuracy and variability of tumour burden measurement on multi-parametric MRI ", **Imaging Network Ontario (ImNO) Symposium**, Toronto, Ontario, Canada (March 24-25, 2014).

- **Salarian M.,** Shahedi M., Gibson E., Gaed M., Gomez J. A., Moussa M., Bauman G. and Ward A., "Toward Quantitative Digital Histopathology for Prostate Cancer: Comparison of Inter-Slide Interpolation Methods for Tomour Measurement", **Imaging Network Ontario (ImNO) Symposium**, Toronto, Ontario, Canada (February 4-5, 2013).

- **Salarian M.,** Shahedi M., Gibson E., Gaed M., Gomez J. A., Moussa M., Bauman G. S., and Ward A. D., "Development of Quantitative Digital Histopathology methods for Prostate Cancer Tumour Measurements", **London Health Research Day**, London, Ontario, Canada (June 13, 2013).

- **Salarian M.,** Shahedi M., Gibson E., Gaed M., Gomez J. A., Moussa M., Cool D. W., Romagnoli C., Bauman G. S., and Ward A. D., "Imaging Validation and Quantitative Pathology for Prostate Cancer Treatment Planning: Shape Interpolation Methods for Tumour Measurement", **Oncology Research and Education Day**, London, Ontario, Canada (June 21, 2013).

- **Salarian M.,** Shahedi M., Gibson E., Gaed M., Gomez J. A., Moussa M., Cool D. W., Romagnoli C., Bauman G. S., and Ward A. D., "Imaging Validation

and Quantitative Pathology for Prostate Cancer Treatment Planning: Shape Interpolation Methods for Tumour Measurement", **Canadian Cancer Research Conference**, Toronto, Ontario, Canada (November 3-5, 2013).

- **Salarian M.,** Shahedi M., Gibson E., Gaed M., Gomez J. A., Moussa M., Bauman G. and Ward A., "Toward Quantitative Digital Histopathology for Prostate Cancer: Comparison of Inter-Slide Interpolation Methods for Tumour Measurement", **5th Annual "Imaging Applications in Prostate Cancer" Workshop**, London, Ontario, Canada (November 16, 2012).

Journal Paper:
- **Salarian M.,** Shahedi M., Gibson E., Gaed M., Gomez J. A., Moussa M., Cool, D., Romagnoli, C., Bauman G. and Ward A., "Toward Quantitative Digital Histopathology for Prostate Cancer: Comparison of Inter-Slide Interpolation Methods for Tumour Measurement", **SPIE Journal of Medical Imaging**, 2014 (in preparation).